

From FFB Starbursts at Cosmic Dawn to Quenching at Cosmic Morning: Hi-z Galaxy Bimodality

Avishai Dekel^{1*}, Nir Mandelker¹, Zhaozhou Li¹, Zhiyuan Yao¹, Bocheng Zhu¹, Sharon Lapiner¹, Dhruva Dutta Chowdhury¹, Omri Ginzburg¹

¹*Racah Institute of Physics, The Hebrew University, Jerusalem 91904 Israel*

16 June 2025

ABSTRACT

We propose a mass-dependent bimodality in the early evolution of galaxies. The massive track connects the super-bright galaxies at cosmic dawn ($z > 8$) to the super-massive quiescent galaxies and black holes (BHs) at cosmic morning ($z \sim 4-7$). The dark-matter halos $> 10^{10.5} M_{\odot}$ at $z = 10$ are expected to undergo feedback-free starbursts (FFB) with high star-formation efficiency in dense star clusters within compact galaxies. The less massive halos avoid FFB and form stars gradually under stellar feedback, leading to the peak star-forming galaxies at cosmic noon ($z \sim 1-3$). The FFB and non-FFB halos originate from $> 4\sigma$ and $2-3\sigma$ density peaks, respectively. The post-FFB galaxies quench their star formation soon after the FFB phase and remain quiescent due to (a) gas depletion by the FFB starbursts and outflows, (b) compaction events driven by angular-momentum loss in colliding streams within the high-sigma-peak FFB halos, (c) turbulent circum-galactic medium (CGM) that suppresses feeding by cold streams, and (d) BH feedback, being a key for complete quenching. BH feedback is enhanced by FFB-driven BH seeding and growth. It seems capable of disrupting the streams by generating CGM turbulence or photo-heating, but this remains an open challenge. The cosmic-morning quiescent galaxies are expected to be massive, compact, showing signatures of compaction, outflows and AGN, with a comoving number density $\sim 10^{-5} \text{ Mpc}^{-3}$, comparable to the super-bright galaxies at cosmic dawn and the AGN at cosmic morning. Their UV luminosity function should peak about $M_{\text{UV}} \sim -22$ and contribute $\sim 10\%$ of the galaxies there.

Key words: galaxies: active — galaxies: evolution — galaxies: formation — galaxies: halos — galaxies: high-redshift — galaxies: interactions

1 INTRODUCTION

1.1 Bright Galaxies at Cosmic Dawn

Observations using JWST reveal a very interesting excess of bright galaxies at “cosmic dawn”, in the redshift range $z = 8-15$ (and possibly beyond), compared to the predictions of standard models within the Λ CDM cosmological framework, that were largely extrapolated from lower redshifts (e.g., Naidu et al. 2022; Haslbauer et al. 2022; Finkelstein et al. 2022, 2023; Boylan-Kolchin 2023; Donnan et al. 2023b,a; Labbé et al. 2023; Bouwens et al. 2023; Mason et al. 2023; Lovell et al. 2023; Adams et al. 2023; Pérez-González et al. 2023; Arrabal Haro et al. 2023; Wilkins et al. 2023; Yung et al. 2024).

Such an excess may partly arise if one assumes a particularly high luminosity-to-mass ratio, which could originate from (a) low dust attenuation (Fiore et al. 2023; Ferrara et al. 2023; Ziparo et al. 2023), (b) a top-heavy stellar initial mass function (IMF) (Zackrisson et al. 2011; Inayoshi et al. 2022; Steinhardt et al. 2023; Harikane et al. 2023a), (c) UV from active galactic nuclei (AGN) (Tacchella et al. 2023; Grudić &

Hopkins 2023; Yung et al. 2024), or (d) a bias due to a fluctuative star-formation history (SFH) at the declining bright end of the galaxy luminosity function (Sun et al. 2023a,b). The excess may alternatively arise by modifying the basic Λ CDM scenario, e.g., by a fine-tuned early dark energy phase (Klypin et al. 2021).

However, such a luminosity excess or changes to the basic framework do not need to be advocated, because an excess in the stellar masses themselves is naturally expected in the high-density conditions at cosmic dawn based on a straightforward physical model within the Λ CDM framework. It predicts high star-formation efficiency due to *feedback-free starbursts* (FFB) in thousands of star clusters within early compact galaxies (Dekel et al. 2023; Li et al. 2024). The trivial key idea is that when the gas density is above a threshold of $n \sim 3 \times 10^3 \text{ cm}^{-3}$, the free-fall star formation is largely complete in ~ 1 Myr, before the onset of suppressive feedback from supernovae and stellar winds from the massive stars with lifetimes of a few Megayears. At moderately low metallicities, such a density is also associated with a cooling time < 1 Myr that guarantees a short ~ 1 Myr burst followed by a feedback-free window of opportunity. Once the surface density is also above a threshold, $\Sigma \sim 3 \times 10^3 M_{\odot} \text{ pc}^{-2}$, the radiative feedback is confined by

* E-mail: dekel@huji.ac.il

the self-gravity of the star-forming clouds and does not suppress the star-formation rate (SFR) in the first free-fall times (Menon et al. 2023; Grudić & Hopkins 2023). The FFB phase is predicted to favorably occur at $z > 8$ in halos of masses $\sim 10^{11} M_{\odot}$ and to last for ~ 100 Myr with an average SFR $\sim 50\text{--}100 M_{\odot} \text{ yr}^{-1}$. The SFH is predicted to be bursty, consisting of several generations of ~ 10 Myr, each starting with a burst followed by a quenched period. The metallicity and dust attenuation are predicted to be low. Together, these features also contribute to the elevated brightness which has been primarily caused by the suppressed feedback.

A hint that is potentially consistent with the FFB predictions is provided by JWST observations using gravitational lensing, which reveal high-redshift galaxies, possibly disks, where the star formation is predominantly in massive, dense star clusters (Vanzella et al. 2023; Claeysens et al. 2023; Mowla et al. 2024; Adamo et al. 2024; Fujimoto et al. 2024; Messa et al. 2024). The detailed relation between these observed systems and the FFB scenario is yet to be investigated (Mayer et al. 2024), and is beyond the scope of the current paper.

1.2 Massive Quiescent Galaxies at Cosmic Morning

The focus of the current paper is the growing evidence from JWST observations for an excess of massive quiescent galaxies several hundred million years after the FFB bright phase at cosmic dawn, in the period we term “cosmic morning”, $z = 4\text{--}7$ (Carnall et al. 2023b,a, 2024; de Graaff et al. 2024a; Weibel et al. 2024; Wang et al. 2024; Setton et al. 2024; Antwi-Danso et al. 2025). The preliminary stellar mass estimates of these galaxies are in the ball park of $M_{*} \sim 10^{10.5} M_{\odot}$, sometimes even $10^{11} M_{\odot}$. With a global, integrated star-formation efficiency (SFE) of ~ 0.1 at cosmic morning (the ratio of stellar mass to baryonic mass that has been accreted onto the halo), the corresponding halo masses are expected to be of $M_{\text{v}} \gtrsim 10^{12} M_{\odot}$. The observed galaxies are typically compact, with a stellar half-mass radius of $R_{\text{e}} \sim 200$ pc, and with a high stellar surface density $\Sigma > 10^4 M_{\odot} \text{ pc}^{-2}$ (e.g. Fig. 3 of Weibel et al. 2024). The number density of such galaxies seems to be one-to-two orders of magnitude above the expectations from simulations (e.g. Fig. 6 of Weibel et al. 2024), in the ball park of the excess of bright galaxies at cosmic dawn, namely at a level of $n(> M_{\text{v}}) \sim 10^{-5} \text{ Mpc}^{-3}$.

The spectra of these galaxies, under certain assumptions (e.g., concerning metallicity and dust), are used to deduce the star-formation histories. In particular, the NIRSpc/PRISM spectra reveal deep Balmer absorption lines and a strong spectral break at a rest-frame wavelength of 4000\AA , indicating a lack of star formation in the recent history under simultaneous modeling with NIRCcam and MIRI photometry. Figure 1 shows examples of SFHs that were derived from such galaxies by different authors. The characteristic finding is that most of the stars were formed at cosmic dawn, $z \sim 8\text{--}11$, likely in a massive peak of duration $100\text{--}200$ Myr, followed by relatively abrupt quenching of star formation, which is maintained till the detection time at cosmic morning. While the exact properties of the early peaks of star formation that are deduced by cosmic archaeology are less solid than the subsequent quiescent period, one cannot resist the temptation to identify these early SFR peaks with the excessively bright galaxies observed at cosmic dawn with similar abundances. The high stellar

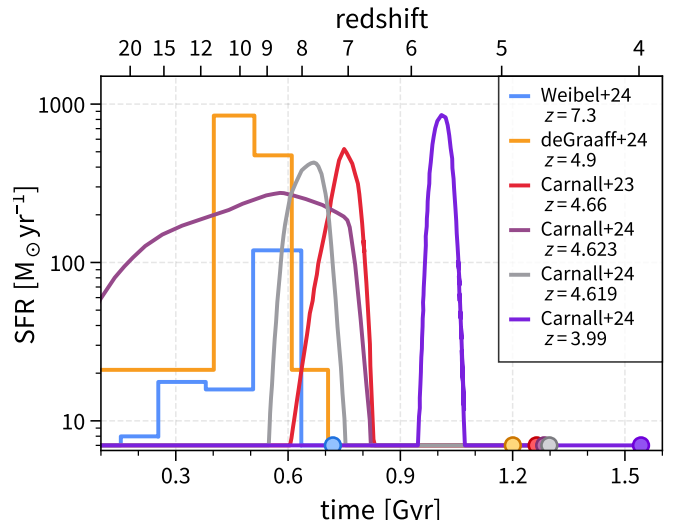


Figure 1. FFB-like starbursts in the histories of massive quiescent galaxies. Shown are star formation histories as estimated from the spectra of six characteristic massive quiescent galaxies observed by JWST at cosmic morning, $z = 4\text{--}7$. The galaxies are ZF-UDS-6496 at $z = 3.99$ (Carnall et al. 2024), PRIMER-EXCELS-117560 at $z = 4.619$ (Carnall et al. 2024), PRIMER-EXCELS-109760 at $z = 4.623$ (Carnall et al. 2024), GS-9209 at $z = 4.66$ (Carnall et al. 2023b), RUBIES-EGS-QG-1 at $z = 4.9$ (de Graaff et al. 2024a), and RUBIES-UDS-QG-z7 at $z = 7.3$ Weibel et al. (2024). Each recovered SFH seems to consist of a starburst of a global duration $100\text{--}200$ Myr, at a level of a few hundred $M_{\odot} \text{ yr}^{-1}$, followed by a robust quiescent period of several hundred Megayears till the observed time. The crudely estimated stellar masses are between $10^{10.3} M_{\odot}$ and $10^{11} M_{\odot}$ for RUBIES-UDS-QG-z7 and RUBIES-UDS-QG-1 respectively. The surface densities are well above $10^4 M_{\odot} \text{ pc}^{-2}$ (Weibel et al. 2024). The estimated cosmological number density of these galaxies is between 10^{-6} and 10^{-4} Mpc^{-3} , well above the expectations from current cosmological simulations (Weibel et al. 2024).

masses of these quiescent galaxies are indeed consistent with the high stellar masses produced at cosmic dawn due to high global star-formation efficiency in dense clusters within compact galaxies along the lines of the FFB scenario (Dekel et al. 2023; Li et al. 2024).

1.3 Bimodality and Quenching

Later in time, “cosmic noon” at $z \sim 1\text{--}3$ is known to be the peak period of massive star-forming galaxies (SFGs), where the cosmological star-formation density reaches a maximum level (Madau & Dickinson 2014). At this epoch, the typical forming halos are of mass $M_{\text{v}} \sim 10^{11\text{--}12} M_{\odot}$, defining the “golden mass” of galaxy formation (Dekel et al. 2019), expressed as a peak in the commonly quoted stellar-to-halo mass ratio (Behroozi et al. 2013; Moster et al. 2018; Behroozi et al. 2019). The emerging questions are how the cosmic-morning quiescent galaxies, and how the latter relate to the super-luminous galaxies at cosmic dawn.

Here we attempt to understand the evolutionary tracks of massive galaxies from cosmic dawn through cosmic morning to cosmic noon. We propose a bi-modality as a function of mass into massive galaxies that undergo an FFB phase at cosmic dawn followed by severe quenching during the post-FFB phase at cosmic morning, and galaxies of somewhat lower masses that do not undergo an FFB phase and evolve to SFGs at cosmic noon.

The challenging issue is to understand the post-FFB quenching mechanism. What gives rise to the end of the FFB phase? What causes the abrupt quenching? What is responsible for the maintenance of the long-term, almost-complete quenching? In turn, what is responsible for the peak of SFR at cosmic noon?

To help answer these questions, we consider several processes that favorably occur at high redshifts and may be relevant. Most of them tend to take place near or above a threshold halo mass, comparable to the golden mass. They include (a) effective supernova feedback at $M_v < 10^{11.8} M_\odot V_{100}^3 (1+z)^{-3/2}$ (Dekel & Silk 1986), (b) virial shock heating of the circumgalactic medium (CGM) at $M_v > 10^{11.8} M_\odot$ (Dekel & Birnboim 2006), (c) feeding of galaxies by cold streams at $z > 1$ (Dekel & Birnboim 2006; Dekel et al. 2009), enhanced by entrainment of hot CGM gas through turbulent radiative mixing layers (Aung et al. 2024). (d) compaction events at $M_v \sim 10^{11.3} M_\odot$ (Zolotov et al. 2015; Lapiner et al. 2023), and (e) formation of post-compaction long-lived disks and rings at $M_v > 10^{11.2} M_\odot$ (Dekel et al. 2020a,b).

1.4 Black Holes and AGN Feedback

A key relevant process of distinct importance for quenching is AGN feedback associated with rapid black-hole (BH) growth, also seen to be mostly relevant at cosmic noon above a threshold mass $M_v > 10^{11.8} M_\odot$ (Förster Schreiber et al. 2019). This onset of BH growth may be triggered by a compaction event, and reflect the transition from the low-mass halo regime where supernova feedback suppresses the BH growth to the massive-halo regime where the CGM is hot (Dekel et al. 2019; Lapiner et al. 2021).

JWST observations at cosmic morning reveal the existence of central massive black holes of masses $10^{6-8} M_\odot$ and excessively high BH-to-stellar mass ratios of ~ 0.01 (Harikane et al. 2023a; Übler et al. 2023; Maiolino et al. 2024), compared to the standard values of $10^{-4} - 10^{-3}$ at lower redshifts (Reines & Volonteri 2015). A feasibility study (Dekel et al. 2025) indicates that the FFB scenario may provide a natural setting for such a rapid black hole growth. This involves the formation of seed BHs by sped-up core collapse in the young, rotating FFB star-clusters, followed by migration driven by dynamical friction to the galactic-disk centers where super-massive BHs first grow by mergers, overcoming gravitational-wave recoils. A post-FFB accretion phase onto the merger-driven massive central BH can boost the accretion-driven AGN feedback in these galaxies, potentially resulting in a major quenching mechanism.

The paper is organized as follows. In §2 we propose a bimodality into two different evolutionary tracks, for post-FFB galaxies and non-FFB galaxies. In §3 to §6 we discuss the possible quenching mechanisms that may be responsible for the post-FFB quiescent galaxies and the interplay between them. In particular, in §3 we address compaction-driven quenching, in §4 we focus on the role of AGN feedback in the quenching, in §5 we evaluate possible ways to suppress gas supply by cold streams for complete quenching, also largely driven by AGN feedback, and in §6 we consider the particularly efficient quenching in post-FFB galaxies. In §7 we discuss observable predictions for the quiescent galaxies. In §8 we summarize our results and conclude.

2 BIMODAL EVOLUTIONARY TRACKS

The conditions for a halo to undergo FFB hints for a division of the halo population into two different evolutionary tracks, the FFB track and the non-FFB track. These tracks are primarily distinguished by halo mass, or equivalently by the rareness of the halo as a peak in the density fluctuation field. This can be deduced from Fig. 2, which addresses the evolution of galaxies in the plane of halo mass versus redshift.

Figure 2 first displays three examples of average growth tracks for halo masses that have a range of values at a given redshift, $M_v = M_0 \simeq 10^{9.8}, 10^{10.5}$ and $10^{11.2} M_\odot$ at $z = z_0 = 10$. The average mass growth is computed based on the simple analytic expression derived in Dekel et al. (2013) in a straightforward way based on the invariant timescale in the Press-Schechter (PS) and Extended Press Schechter (EPS) theory (Press & Schechter 1974; Bond et al. 1991),

$$M_v(z) = M_0 e^{-\alpha(z-z_0)}, \quad \alpha \simeq 0.79. \quad (1)$$

This expression was derived in the Einstein-deSitter regime at high redshifts $z > 1$, and it has been shown to be a good approximation in comparison with cosmological simulations (see also Wechsler et al. 2002; Zhao et al. 2009).

Eq. (1) is derived by integrating eq. 7 of Dekel et al. (2013), which boils down to

$$\frac{\dot{M}_v}{M_v} = s_{10} M_{v,12}^\beta (1+z)_{10}^{5/2}, \quad (2)$$

with the simplifying approximation $\beta = 0$ (as in eq. 8 there). The power β depends on the slope of the power spectrum of density fluctuations near the mass scale of interest. A value of $\beta \simeq 0.14$ was advocated in Dekel et al. (2013), and shown to provide a best fit to simulations for massive galactic halos at cosmic noon. However, we find that $\beta = 0$ (actually $\beta \simeq 0.03$) provides a better approximation for the halos of $\sim 10^{11} M_\odot$ at $z > 5$. This is verified in comparison to simulations by Zhao et al. (2009), which are reliable out to $z \sim 10$. We thus adopt $\beta = 0$, and thus gain simplicity in eq. (1) and the subsequent analysis. In eq. (2) the halo mass is $M_v \equiv 10^{12} M_\odot M_{v,12}$ and $1+z \equiv 10(1+z)_{10}$. The normalization factor in eq. (2) is calibrated from simulations to be $s_{10} \simeq 9.5 \text{ Gyr}^{-1}$, and this translates in the Einstein-deSitter regime to the value of α quoted in eq. (1).

Figure 2 shows in the background of the same diagram the curves corresponding to $N\sigma$ peaks in the Gaussian random field of linear density fluctuations, based on the Press-Schechter formalism (Press & Schechter 1974), for $N = 2-5$. We learn that the middle growth curve, which corresponds to $M_v = 10^{10.5} M_\odot$ at $z = 10$, roughly matches the 4σ -peaks curve in a broad redshift range, $z \geq 5$. The upper growth curve of higher-mass halos, with $M_v = 10^{11.2} M_\odot$ at $z = 10$, is close to the 5σ -peaks curve. Thus, these high-mass halos at and above the middle growth curve correspond to rare high-sigma peaks.

Also shown in the background of Fig. 2 are contours of constant comoving number density of halos, $n = 10^{-6}$ and 10^{-4} Mpc^{-3} . These contours confine the middle growth curve at $z \leq 11$. We caution that the exact interplay between the contours of constant n and constant N depends on the assumed value of β in the specific accretion rate of eq. (2).

The number densities of the halos above the middle growth curve match the low abundance of the super-luminous galaxies

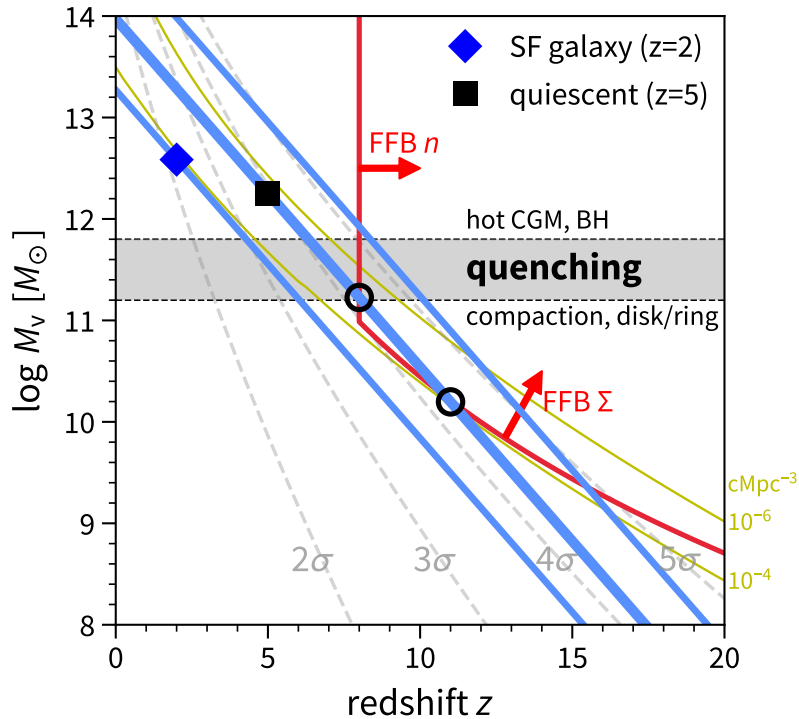


Figure 2. Bimodal evolutionary tracks of galaxies: FFB and non-FFB. Shown (blue lines) are average growth tracks for halos that at $z_0 = 10$ have masses $M_v = 10^{9.84}, 10^{10.54}, 10^{11.24} M_\odot$. The threshold for FFB in a disk (red curve) consists of thresholds for gas density n and surface density Σ following Fig. 6 of Dekel et al. (2023). The $N\sigma$ peaks in the density fluctuation field (dashed grey curves) indicate that the middle halo is roughly a 4σ peak. Galaxy number densities of 10^{-4} and 10^{-6} Mpc^{-3} are marked (thin green curves), confining the middle halo at $z \leq 11$. We learn that the halos of mass $\geq 10^{10.5} M_\odot$ at $z = 10$ ($\geq 4\sigma$ peaks) undergo an FFB phase, while halos of lower masses (lower- σ peaks) never become FFB. The “fiducial”, most abundant FFB galaxies, those near the middle blue curve, enter the FFB phase near $z \sim 11$ (right black circle) and exit at $z \sim 8$ (left black circle), after ~ 170 Myr and when $M_v \gtrsim 10^{11} M_\odot$. Soon after, the fiducial FFB halos cross the “golden mass” (Dekel et al. 2019) $M_v \gtrsim 10^{11.5} M_\odot$, between the horizontal dashed lines, that mark the onset of quenching by several different mechanisms. These include a hot CGM (Dekel & Birnboim 2006), wet compaction events (Zolotov et al. 2015; Lapiner et al. 2023), the rapid growth of super-massive BHs and AGN (Lapiner et al. 2021), as well as long-lived extended disks and rings (Dekel et al. 2020a,b). The quenching of the FFB galaxies is efficient because of the intense compaction activity in high-sigma halos (Dubois et al. 2012) and the compaction-driven AGN feedback (Lapiner et al. 2021) that is boosted by FFB BH seeding and growth (Dekel et al. 2025). By cosmic morning, at $z \sim 5$, these quenching mechanisms lead to quiescent galaxies of stellar mass $M_* \sim 10^{10.5} M_\odot$ in halos of $M_v \gtrsim 10^{12} M_\odot$ (black square), as observed. These halos eventually become quiescent groups and clusters of galaxies. The lower-sigma halos with masses below the FFB threshold accrete gas and form stars more gradually as they grow. At cosmic noon, $z \sim 2-3$, when these halos are above $10^{12} M_\odot$, cold gas streams penetrate efficiently through the hot CGM (Dekel et al. 2009), boosted by entrainment of hot CGM gas onto the cold streams (Aung et al. 2024), giving rise to star forming galaxies at their peak (blue diamond). At $z \leq 1$, cold streams do not penetrate the hot halos (Dekel & Birnboim 2006, Fig. 7), such that these galaxies end up with lower SFRs.

as observed using JWST at cosmic dawn, with halo masses of $\sim 10^{11} M_\odot$ based on the Λ CDM halo mass function shown in Fig. 3, given the observed number density of $n \sim 10^{-5} \text{ Mpc}^{-3}$ (Finkelstein et al. 2023). We will see in Fig. 3 below that these number densities similarly match the abundance of the massive quiescent galaxies at cosmic morning, with $M_v \sim 10^{12} M_\odot$ (Weibel et al. 2024). On the other hand, the lower growth curve of lower masses shown in Fig. 2, those with $M_v = 10^{9.8} M_\odot$ at $z \approx 10$, is below the 4σ -peaks curve, coinciding with the 3σ curve at $z \approx 4$ and with the 2σ curve at $z \approx 2$. These more typical (but still high) peaks match the higher abundance of the typical star-forming galaxies at cosmic noon.

Next, and most important, Fig. 2 displays the threshold for FFB according to the disk version of the FFB scenario, following Fig. 6 of Dekel et al. (2023). The vertical part of the threshold at $z \sim 8$ refers to the critical gas number density, $n \sim 3 \times 10^3 \text{ cm}^{-3}$, in the star-forming clouds within the disks. Higher densities allow for free-fall collapse times of ~ 1 Myr and thus efficient feedback-free star formation prior to the onset of feedback by supernovae and stellar winds. This threshold stems from eq. 42 of Dekel et al. (2023), where the density in

the clumps is estimated to be

$$n_c = 5.6 \times 10^3 \text{ cm}^{-3} c \lambda_{0.025}^{-3} (1+z)_{10}^3. \quad (3)$$

Here $\lambda \equiv 0.025 \lambda_{0.025}$ is the contraction factor from the halo to the disk, which is partly associated with the halo spin parameter (Fall & Efstathiou 1980; Jiang et al. 2019), and $c > 1$ is the density contrast between the star-forming clumps and the background density in the disk. Such densities, with moderately low metallicities of $Z \sim 0.02 Z_\odot$, also correspond to cooling on free-fall timescales which permits a short starburst followed by a well-defined window free of feedback (Dekel et al. 2023, eq. 12). The other part of the threshold mass that declines with redshift refers to the critical surface density, $\Sigma \sim 3 \times 10^3 M_\odot \text{ pc}^{-2}$, above which the stellar radiative pressure is balanced by the self-gravity of the clouds, minimizing the suppression of star formation by radiative feedback (Menon et al. 2023; Grudić & Hopkins 2023; Menon et al. 2024). This threshold, based on eqs. 62 and 67 of Dekel et al. (2023), is roughly

$$M_{v,10.8} (1+z)_{10}^{6.2} > 0.8, \quad (4)$$

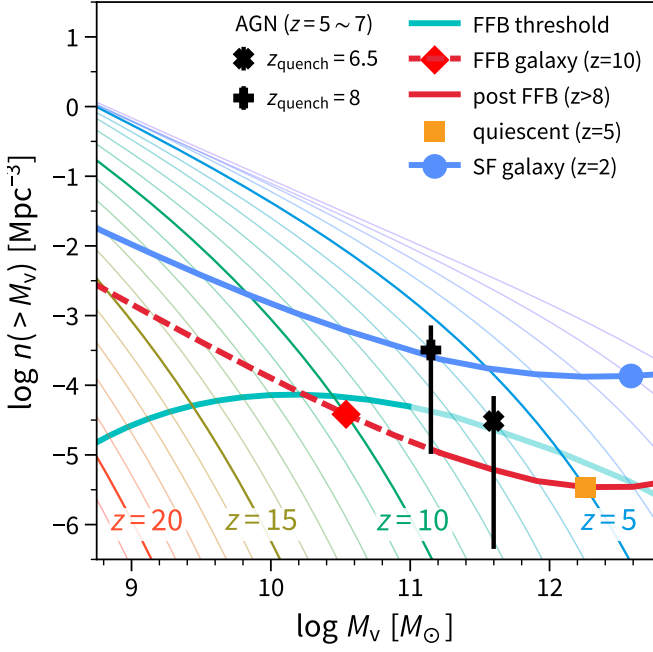


Figure 3. Two evolutionary tracks in the plane of halo mass function, comoving number density versus halo mass, complementing Fig. 2. The halo mass functions at different redshifts are shown in the background, based on Watson et al. (2013). The red curve refers to the evolving fiducial FFB halos that reach $\sim 10^{10.5} M_{\odot}$ at $z = 10$ (roughly 4σ peaks). The cyan curve is the threshold for FFB, $M_{v,10.8}(1+z)_{10}^{6.2} = 0.8$. The curves stretching on the left of $z = 8$ (dashed, $M_v < 10^{11.2} M_{\odot}$) refer to the FFB phase, and the curves to the right of $z = 8$ (solid, $M_v > 10^{11.2} M_{\odot}$) correspond to the post-FFB quiescent phase. The typical halo number density in the post-FFB zone is $n \gtrsim 10^{-5} \text{ Mpc}^{-3}$. The upper horizontal zone near $n \sim 10^{-3} \text{ Mpc}^{-3}$ corresponds to the non-FFB evolution track reaching the peak of star-forming galaxies at $z \sim 2$. Colored symbols mark the fiducial starbursting FFB halos at cosmic dawn ($M_v \sim 10^{10.5} M_{\odot}$ at $z \sim 10$ where $n \sim 10^{-4.3} \text{ Mpc}^{-3}$), the fiducial quiescent halos at cosmic morning ($M_v \sim 10^{12.2} M_{\odot}$ at $z \sim 5$ where $n \sim 10^{-5.3} \text{ Mpc}^{-3}$), and the fiducial non-FFB star-forming galaxies at cosmic noon ($M_v \sim 10^{12.6} M_{\odot}$ at $z \sim 2$ where $n \sim 10^{-3.5} \text{ Mpc}^{-3}$). Shown for comparison (black symbols) are number densities of AGN observed by JWST (Harikane et al. 2023b) at $z = 5-7$ in quiescent galaxies brighter than the corresponding predicted UV magnitudes of post-FFB galaxies with quenching onset at $z_{\text{quench}} = 8$ or 6.5 (see Fig. 10). The abundance of BHs is in the ballpark of that predicted for the quiescent galaxies when the onset of quenching is at $z \sim 6.5$, and is somewhat higher for higher z_{quench} . (See also the number densities in Fig. 11 below.)

where $M_v \equiv 10^{10.8} M_{\odot} M_{v,10.8}$.

Taking the threshold curve for FFB at face value (which is clearly an over-simplification considered for a qualitative estimate only), we learn from Fig. 2 that the halos of mass $\geq 10^{10.5} M_{\odot}$ at $z = 10$, representing $\geq 4\sigma$ peaks, undergo an FFB phase, while halos of lower masses, which emerge from lower- σ peaks, never become FFB. Thus, the most abundant FFB galaxies at $z \sim 10$ are those of $M_v \gtrsim 10^{10.5} M_{\odot}$, which we therefore refer to as the “fiducial” FFB galaxies. We see from Fig. 2 that they enter the FFB phase near $z \simeq 11$, while the more massive, less abundant halos enter the FFB phase at higher redshifts. This defines a bi-modality between galaxies that undergo FFB and galaxies that do not, separated near halo mass $M_v \sim 10^{10.5} M_{\odot}$ at $z \sim 10$, namely near 4σ peaks.

The FFB phase ends when the density drops below the critical value at $z \sim 8$. For the fiducial FFB galaxies the overall

duration of the FFB phase, between the two black open circles in Fig. 2, is ~ 170 Myr, similar to the estimate in Dekel et al. (2023) (see also Fig. 9 of Li et al. 2024). At the end of the FFB phase, the fiducial halos are somewhat more massive than $10^{11} M_{\odot}$.

Soon after the end of the FFB phase, the fiducial FFB halos reach the “golden mass” (Dekel et al. 2019), in the vicinity of $M_v \sim 10^{11.5} M_{\odot}$, which marks the onset of quenching of star formation by several different quenching mechanisms, to be discussed below. These include the onset of a hot CGM (Dekel & Birnboim 2006), the rapid growth of super-massive black holes and AGN (Lapiner et al. 2021), wet compaction events (Zolotov et al. 2015; Lapiner et al. 2023), and the formation of long-lived extended disks and rings (Dekel et al. 2020a,b). The range of halo masses expected at the onset of quenching is crudely marked by a shaded area between horizontal lines in Fig. 2. We learn that the fiducial post-FFB halos start quenching soon after $z \sim 8$. By $z \sim 5$, they grow above $10^{12} M_{\odot}$, where all the quenching mechanisms mentioned above have been potentially at play. If the post-FFB quenching is indeed efficient, both in terms of abrupt onset and long-term maintenance, these galaxies would resemble the observed massive quiescent galaxies at cosmic morning. With an integrated global star-formation efficiency SFE of 0.2 to 1 in the FFB phase (Li et al. 2024), where $M_v \sim 2 \times 10^{11} M_{\odot}$, and with low SFR since then in the post-FFB phase, the stellar mass is expected to be roughly constant at $M_* \gtrsim 10^{10} - 10^{10.5} M_{\odot}$. A similar estimate of $M_* \sim 10^{10.5} M_{\odot}$ is obtained from the halo mass at the quiescent phase assuming a stellar-to-halo-mass ratio of 0.1 (Behroozi et al. 2019). These estimates of stellar mass are comparable to the typical observed estimates. As these halos grow further at lower redshifts, they are expected to become the hosts of quiescent groups and clusters of galaxies.

Lower mass halos, which never enter the FFB phase, can accrete gas and form stars gradually as they grow. They enter the quenching regime at $z \leq 7$, but their quenching is likely to be less efficient than in the post-FFB galaxies (see §6.1). At cosmic noon, near $z \sim 2-3$, when these non-FFB halos are above $10^{12} M_{\odot}$, cold gas streams penetrate efficiently through the hot CGM (Dekel et al. 2009; Mandelker et al. 2020a), boosted by entrainment of hot CGM gas onto the cold streams through a turbulent mixing layer (Aung et al. 2024), giving rise to star forming galaxies at the peak of cosmic star formation density. At $z \sim 1$ and later, these galaxies find themselves in the regime where cold streams do not penetrate the hot halos (Dekel & Birnboim 2006; Mandelker et al. 2020a,b; Daddi et al. 2022a,b, Fig. 7), such that they end up with lower SFRs today.

Figure 3 complements Fig. 2 in introducing the two evolutionary tracks of FFB and non-FFB galaxies, focusing on the halo masses and their cosmological number densities. The halo mass functions at different redshifts (separated by $\Delta z = 1$) are plotted in the background based on simulations by Watson et al. (2013). The assumed cosmology is Λ CDM with $\Omega_m = 0.3$, $\Omega_{\Lambda} = 0.7$, $h = 0.7$ and $\sigma_8 = 0.82$, and the halos are assumed to be spherical with a mean density contrast of 200. The red curve refers to the evolving fiducial halos that reach $10^{10.5} M_{\odot}$ at $z = 10$ (roughly 4σ peaks). The cyan curve marks the threshold for FFB due to the surface density criterion, eq. (4), based on Dekel et al. (2023). The curves stretching on the left of $z = 8$ ($M_v < 10^{11.2} M_{\odot}$) refer to the starburst-

ing FFB phase, while the curves extending to the right of $z = 8$ ($M_v > 10^{11.2} M_\odot$) correspond to the subsequent quiescent phase of the post-FFB halos. The typical halo number density for this FFB and post-FFB zone is in the ballpark of $n \sim 10^{-5} \text{Mpc}^{-3}$, highlighting the similar abundances of bright FFB galaxies at cosmic dawn and quiescent post-FFB galaxies at cosmic morning (see also Fig. 11 below), with the associated halo masses growing from $10^{11} M_\odot$ to above $10^{12} M_\odot$.

In Fig. 3, the non-FFB evolutionary track is represented by the upper curve near $n \sim 10^{-3.5} \text{Mpc}^{-3}$, leading to the peak of star-forming galaxies at cosmic noon, with halos above $10^{12} M_\odot$ at $z \sim 2$. Symbols mark the fiducial starbursting FFB halos at cosmic dawn ($M_v \sim 10^{10.5} M_\odot$ at $z \sim 10$ where $n \sim 10^{-4.5} \text{Mpc}^{-3}$), the fiducial quiescent halos at cosmic morning ($M_v \sim 10^{12.25} M_\odot$ at $z \sim 5$ where $n \sim 10^{-5.4} \text{Mpc}^{-3}$), and the fiducial non-FFB star-forming galaxies at cosmic noon ($M_v \sim 10^{12.6} M_\odot$ at $z \sim 2$ where $n \sim 10^{-3.9} \text{Mpc}^{-3}$).

3 COMPACTION-DRIVEN QUENCHING

If the evolutionary track of FFB galaxies as envisioned based on Fig. 2 is valid, these galaxies are supposed to quench rather abruptly over ~ 100 Myr soon after the FFB phase, and subsequently the quiescence should be maintained for at least several hundred Megayears. As seen in Fig. 2, the post-FFB halo masses are near the golden mass of galaxy formation (Dekel et al. 2019), between 10^{11} and $10^{12} M_\odot$, above which several different quenching mechanisms are expected to be at play. Expanding on an earlier discussion in Dekel et al. (2019), we discuss in this and following sections the main mechanisms, their mass dependence, their potential mutual interplay, and their possible role in triggering quenching and maintaining it. We discuss here compaction-driven quenching (§3), briefly address AGN feedback (§4), focus on the challenge of stopping the cold streams (§5), and emphasize the possible dependence of the quenching mechanism on having an earlier FFB phase (§6).

3.1 Golden mass between supernova feedback and hot CGM

At cosmic morning, the golden mass seems to be above the maximum halo mass for effective supernova feedback on the scale of the galaxy as a whole, which can be estimated by (Dekel & Silk 1986)

$$M_v \simeq 3.3 \times 10^{10} M_\odot V_{100}^3 (1+z)_7^{-3/2}, \quad (5)$$

where $V_v = 100 \text{ km s}^{-1} V_{100}$ is the halo virial velocity and $1+z=7$ ($(1+z)_7$). To the extent that this estimate is valid, we may not expect supernova feedback to play a direct major role in the overall quenching of post-FFB galaxies where $M_v \geq 10^{11} M_\odot$ (Boylan-Kolchin 2023; Dekel et al. 2023), the way they do in less massive galaxies.

In more massive halos, the golden mass serves as a threshold for a hot CGM near the virial temperature, bounded by a stable virial shock (Birnbom & Dekel 2003; Dekel & Birnbom 2006). At low redshifts, $z < 2$, where the accretion tends to be more isotropic, the hot CGM suppresses the gas supply to the galaxy and thus limits the SFR. However, at cosmic noon, $z \geq 2$, the hot CGM is expected to be penetrated by

narrow cold streams from the cosmic web (Fig. 7 of Dekel & Birnbom 2006; Kereš et al. 2009), as seen in cosmological simulations (Dekel et al. 2009). At such epochs, the hot CGM is not expected to serve as a direct quenching mechanism. In fact, the cold streams are likely to be intensified by entrainment from the hot CGM, which is partly fed by recycling of gas from the galaxy (Aung et al. 2024). This gives rise to the observed peak of SFR density as a function of redshift (Madau & Dickinson 2014) and the associated observed peak of stellar-to-halo mass ratio as a function of mass at cosmic noon (Behroozi et al. 2013; Moster et al. 2018; Behroozi et al. 2019). In general, supernova feedback at small masses and a hot CGM at large masses confine the golden mass in between.

3.2 Direct quenching by compaction events

Cosmological simulations (Zolotov et al. 2015; Lapiner et al. 2023) and observations (Barro et al. 2013; van Dokkum et al. 2015; Barro et al. 2017) reveal that most galaxies undergo wet-compaction events throughout their histories. These events induce major transitions in the galaxy properties, and in particular trigger quenching of star formation in several different ways. The compaction processes are due to drastic angular-momentum losses, about half of which are caused by mergers and the rest by colliding counter-rotating streams, recycling fountains from the galactic disks, and other mechanisms. The major deep compaction events to “blue nuggets”, those that trigger a decisive long-term quenching process and a transition from central dark-matter to baryon dominance, tend to occur near the golden mass at all redshifts. This is seen in simulations (Tomassetti et al. 2016) and in machine-learning-aided comparisons to observations (Huertas-Company et al. 2018). This preferred mass scale for major compaction events seems to be due, at least partly, to the two physical processes mentioned above of supernova feedback and hot CGM (with AGN feedback - see below), which tend to suppress compaction attempts at lower and higher masses. At cosmic dawn, the FFB halos are indeed of masses $\sim 10^{11} M_\odot$, in the vicinity of the golden mass, and they correspond to high-sigma peaks of $> 4\sigma$, which tend to have more frequent and stronger compaction events (see §6.1 below).

The compaction events drive quenching in several different ways, directly and indirectly. Quite straightforwardly, as the gas that is pushed to the galaxy center triggers a central starburst in the form of a blue nugget, it causes central gas depletion due to star formation and the associated outflows, thus leading to inside-out quenching (Tacchella et al. 2016a,b). Secondly, compaction events drive the subsequent formation of extended gas disks and rings by new incoming streams (Tacchella et al. 2016b; Dekel et al. 2020b). The compact massive nugget, or bulge, stabilizes the disk/ring against gravitational instability. This suppresses star formation in the outskirts (“morphological quenching”, Martig et al. 2009) and limits the rate of gas supply to the center by instability-driven inward radial transport (Dekel et al. 2020b; Dutta Chowdhury et al. 2024). It turns out that long-lived extended disks are coincidentally favored above the same golden mass due to the fact that merger-driven disk flips become less frequent than the disk orbital time above this mass at all redshifts (Dekel et al. 2020a). This contributes to limiting the gas supply for

star formation in the center and thus generating inside-out quenching.

It remains to be verified to what extent these direct effects of compaction can lead to complete quenching, as observed. Otherwise, complete quenching may require another mechanism, such as enhanced AGN feedback, which can be an indirect outcome of the compaction process (§4 below).

4 BLACK-HOLE GROWTH AND AGN FEEDBACK

4.1 Black-hole growth

A major source of quenching in massive galaxies is commonly assumed to be AGN feedback, driven by the rapid growth of a supermassive central accreting black hole. Observationally at cosmic noon, high-luminosity AGN tend to occur above a threshold mass that is comparable to the golden mass (Förster Schreiber et al. 2018). Based on the NewHorizon cosmological simulations, the onset of BH growth has been shown to originate in a compaction event (Dekel et al. 2019; Lapiner et al. 2021), as follows. Below the golden mass, black-hole growth is suppressed by supernova feedback. Above the golden mass, the central black hole is free to grow once the halo is massive enough to lock the supernova ejecta by its deep potential well and the hot CGM. Once the halo is in this mass range, the BH growth is triggered by a compaction event, which brings gas to the galaxy center and deepens the potential well, making the black hole orbit sink to the galaxy center and thus allowing rapid BH growth by accretion. In turn, the ignited AGN feedback helps keeping the CGM hot and maintaining long-term quenching.

In addition to the general scenario of compaction-driven BH growth, it turns out that the FFB scenario may provide a natural setting for particularly rapid black-hole growth, both through the formation of intermediate-mass BH seeds and their runaway merging into super-massive BHs with high BH-to-stellar mass ratios. The feasibility of this scenario has been addressed by Dekel et al. (2025), as follows. BH seeds can form by core collapse in a few free-fall times within the building blocks of the FFB galaxies, namely, thousands of young, compact, rotating star clusters within each galaxy. The core collapse is sped up by the migration of massive stars to the cluster center due to the young, broad stellar mass function (and more so if the IMF is top heavy). It is expected to be stimulated by a “gravo-gyro” instability (Hachisu 1979) due to internal cluster rotation and flattening within the compact galactic disk that fragmented to form the clusters. BHs of $10^4 M_\odot$ are typically expected in $10^6 M_\odot$ FFB clusters within sub-kpc galactic disks at $z \sim 10$. The orbiting clusters rapidly disrupt each other, generating a smooth stellar disk capable of exerting dynamical friction on the BHs. The BHs then migrate to the galaxy center by dynamical friction in a few 100 Myr, hastened by the compact FFB stellar galactic disk configuration. Efficient mergers of the BH seeds produce $10^{6-8} M_\odot$ BHs with a BH-to-stellar mass ratio ~ 0.01 by $z=4-7$, resembling the JWST observations (Harikane et al. 2023b; Maiolino et al. 2024). Once the central BH has grown to above $10^6 M_\odot$ by this merger-driven process, post-FFB gas accretion can efficiently boost the BH growth further and generate AGN capable of effective feedback.

The wet compaction events can further assist in the post-FFB black-hole growth in three important ways. First, they can prevent core stalling (Read et al. 2006; Goerdt et al. 2006; Kaur & Sridhar 2018; Banik & van den Bosch 2021) in the dynamical-friction-driven inspiral of the BH seeds, by steepening the inner galactic density profile. Second, they can help the final parsec approach (Begelman et al. 1980) by providing central gas. Third, and most critical, they can help overcoming the bottleneck in the initial growth of the central BH that is introduced by gravitational-wave recoils of the merged BH (Madau & Quataert 2004; Blecha & Loeb 2008). Dekel et al. (2025) found that the recoils may be under control if the BHs inspiral within a relatively cold disk, such that their spins tend to be aligned with the orbital angular momentum. However, in more realistic thick disks, the merged BH could avoid ejection by recoil only if the escape velocity from the central galaxy is boosted to a few hundred km s^{-1} by wet compaction events.

4.2 AGN quenching in simulations and observations

The crucial role of AGN feedback in reaching complete compaction-driven quenching over the whole galaxy can be illustrated by comparing cosmological simulations with and without AGN feedback. Figure 4 shows such a comparison, using example galaxies from the VELA simulations with no AGN and the NewHorizon simulations where AGN are incorporated. These simulations and their relevant analyses are described in Lapiner et al. (2023) and Lapiner et al. (2021) and references therein, respectively.

Very briefly, the VELA simulations (Ceverino et al. 2014; Zolotov et al. 2015) utilize the ART AMR code (Kravtsov et al. 1997; Ceverino & Klypin 2009) with ~ 25 pc maximum resolution to zoom in on galactic halos that reach $\sim 10^{12} M_\odot$ at $z \sim 1$. Supernova and radiative stellar feedback are incorporated, as described in appendix A of Lapiner et al. (2023) and in Ceverino et al. (2014), but AGN feedback is not included. The NewHorizon simulation (Dubois et al. 2021), on the other hand, utilizes the RAMSES AMR code (Teyssier 2002) with ~ 40 pc resolution to zoom in on a group of galaxies with eight galaxies of stellar masses above $10^{10} M_\odot$ by $z=0.7$. The subgrid physics incorporates both supernova and stellar feedback as well as black holes with AGN feedback as described in appendix A of Lapiner et al. (2021), in Dubois et al. (2021) and in the NewHorizon website.

We see in Fig. 4 that the compaction events in the VELA simulations with no AGN lead to inside-out quenching. This is quenching in the inner 1 kpc, with a declining SFR and a constant stellar mass in time, but the overall stellar mass keeps rising, namely the quenching of the whole galaxy is incomplete. We learn that the compaction-driven gas consumption, the emergence of a disk/ring, and the hot CGM do trigger quenching in the inner galaxy, but fail to completely shut down the overall star formation. The specific SFR gradually declines from $\text{sSFR} \sim 0.3 \text{ Gyr}^{-1}$ but it remains non-vanishing at $\text{sSFR} \gtrsim 0.1 \text{ Gyr}^{-1}$. On the other hand, when AGN feedback is incorporated in the NewHorizon simulations, the whole galaxy is quenched, with M_* rather constant in time. The specific SFR declines more steeply and reaches low values of $\text{sSFR} \sim 0.01 \text{ Gyr}^{-1}$. Here, the compaction triggers rapid BH growth and AGN feedback, which in turn suppresses further gas supply and allows for the complete quenching.

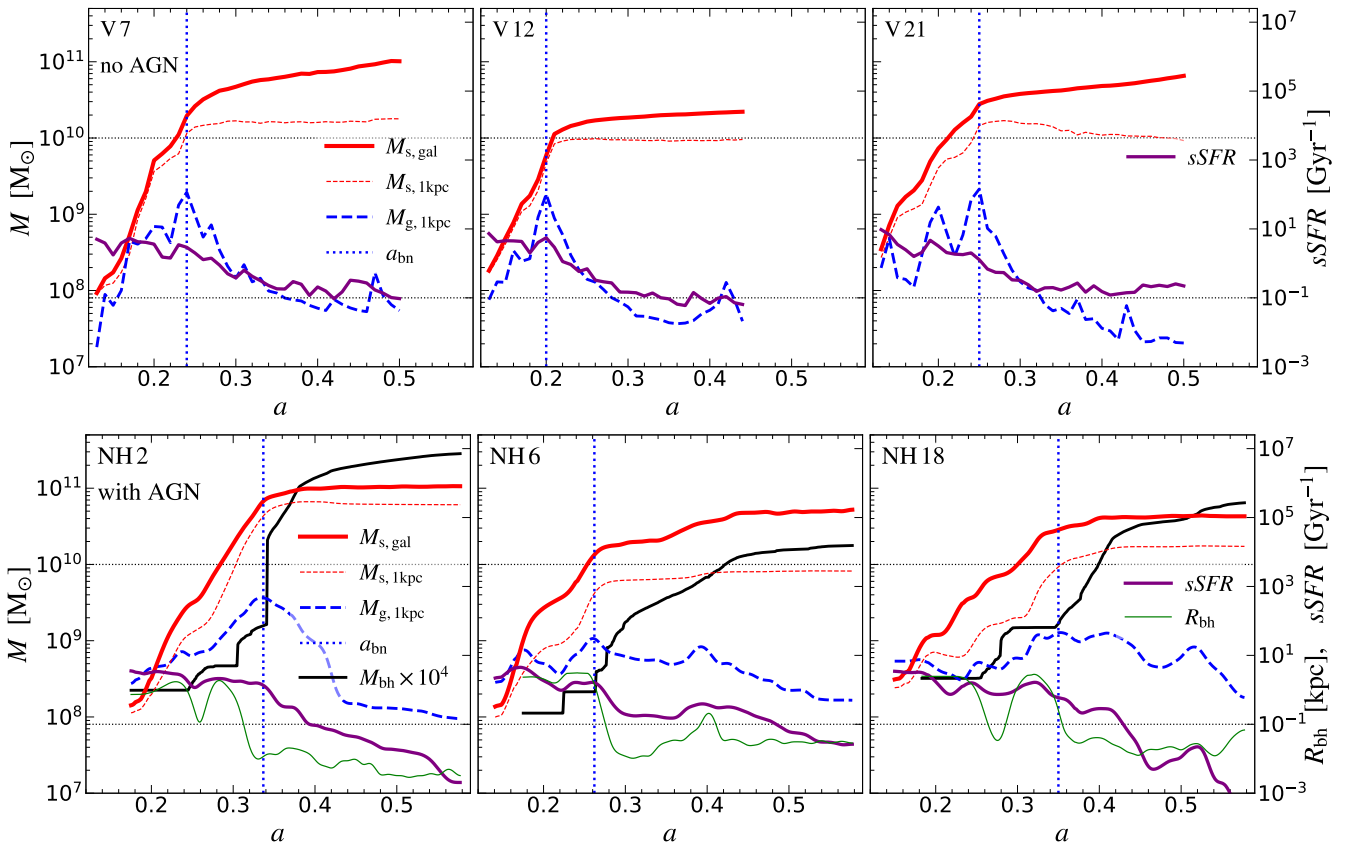


Figure 4. Compaction-driven quenching without (top) and with (bottom) AGN feedback. Shown are the evolution of quantities of interest in the VELA simulations without AGN feedback (Lapiner et al. 2023) (top) and in the NewHorizon simulations that incorporate AGN feedback (Lapiner et al. 2021) (bottom). The compaction event is characterized by the peak in gas mass within the central 1 kpc (blue curve, marked by a vertical line) and the subsequent decay of the BH orbit to the center (Lapiner et al. 2021) (green). Following the compaction, in the presence of AGN the SFR drops (magenta) and the stellar mass (solid red) tends to remain rather constant over the whole galaxy (as well as in the inner 1 kpc, dashed red). Galaxy NH6, with two successive compaction events, shows two successive quenching events. On the contrary, in the absence of AGN feedback, the quenching is only partial, limited to the inner 1 kpc, while the stellar mass over the whole galaxy keeps growing. We learn that AGN feedback is crucial for the deep quenching at cosmic morning, consistent with the findings of other simulations (see text). We thus suspect that the boosted BH growth due to the FFB phase may be a key for post-FFB quenching.

Qualitatively similar results were obtained when comparing other cosmological simulations with and without AGN feedback. For example, the Horizon-AGN and no-AGN simulations (Dubois et al. 2016) and similarly the NIHAO simulations (Blank et al. 2019). They highlight the role of merger-driven AGN activity in leading to complete quenching. de Graaff et al. (2024b), who compared TNG50 simulations with and without AGN feedback at cosmic morning, found that as soon as AGN feedback switches on, the central 1 kpc becomes completely stellar-dominated, with all gas expelled, indicating at least central quenching. We note however that the existing simulations mainly address galaxies at cosmic noon, at $z \lesssim 3$. Extending the conclusions concerning the role of AGN feedback to cosmic morning will require simulations that reliably explore the galaxy and black hole evolution at higher redshifts, resolving the relevant physical processes with sub-pc resolution and appropriate physical recipes.

Observationally, there is potential evidence for outflows and AGN feedback in compact quiescent galaxies at cosmic morning (Onoue et al. 2024; Weibel et al. 2024; de Graaff et al. 2024a; Valentino et al. 2025) and early cosmic noon (Belli et al. 2024; D’Eugenio et al. 2024). These are consistent with compaction-driven AGN feedback as the main quenching mechanism.

5 SHUTOFF OF GAS SUPPLY BY COLD STREAMS

5.1 The challenge of stream disruption

The feeding of massive galaxies at high redshifts is primarily by cold streams from the cosmic web (Dekel & Birnboim 2006; Dekel et al. 2009; Kereš et al. 2009). The average baryonic accretion rate (mostly through streams) onto a halo of mass M_v at z , based on Dekel et al. (2013) (also eq. 31 of Dekel et al. 2023), is

$$\dot{M}_{\text{ac}} \simeq 620 M_{\odot} \text{ yr}^{-1} M_{12}^{1.14} (1+z)_7^{5/2}, \quad (6)$$

where $M_v \equiv 10^{12} M_{\odot} M_{12}$ is the halo virial mass and $1+z \equiv 7(1+z)_7$. The observed quiescent galaxies at cosmic morning, as well as the fiducial post-FFB halos according to Fig. 2, are indeed in the ballpark of $M_v \sim 10^{12} M_{\odot}$ at $z \sim 6$. Thus, the accretion rate onto them is well above the observational estimates of the upper limits on their SFR, which are on the order of $\sim 10 M_{\odot} \text{ yr}^{-1}$. Therefore, a crucial requirement for quenching in these galaxies is that the cold streams are largely disrupted and the cold gas mass flux is greatly reduced before they feed the central galaxy. As we see below, this turns out to be a very non-trivial requirement.

Early work on the purely hydrodynamical evolution of cold streams showed that sufficiently narrow streams, with small

radii that are related to the virial radius as $R_s \lesssim 0.05 R_v$, would fully disrupt in the hot CGM due to Kelvin-Helmholtz instabilities (KHI, Mandelker et al. 2016, 2019; Padnos et al. 2018). However, these instabilities are stabilized by radiative cooling, self-gravity and magnetic fields. When radiative cooling is considered, hot CGM gas cools and condenses onto the stream through a turbulent radiative mixing layer that forms at the interface between the stream and the CGM due to the initial onset of KHI (Mandelker et al. 2020a). This causes the cold gas mass in the streams to grow rather than decline due to KHI, provided the cooling time in the turbulent mixing layer, $t_{\text{cool,mix}}$, is shorter than the timescale for KHI to fully disrupt the stream in the pure-hydro case, hereafter the shearing timescale, t_{shear} . Analogous results were obtained in the context of spherical clouds or planar shear layers (Gronke & Oh 2018; Ji et al. 2019; Gronke & Oh 2020a; Sparre et al. 2020; Fielding et al. 2020; Tan et al. 2021; Kanjilal et al. 2021).

These considerations, confirmed by idealized simulations, yield a critical stream radius above which entrainment of hot CGM gas onto the cold stream dominates over KHI-induced mixing of stream gas into the CGM, such that streams with $R_s > R_{s,\text{crit}}$ are expected to survive the journey to the central galaxy. The critical radius is estimated by (Mandelker et al. 2020a,b)

$$R_{s,\text{crit}} \simeq 0.45 \text{ kpc } \alpha_{0.1} \delta_{100}^{3/2} \mathcal{M}_b \frac{T_{s,4}}{n_{s,0.01} \Lambda_{\text{mix},-22.5}}, \quad (7)$$

where $\delta_{100} \equiv \rho_s / (100 \rho_b)$ is the density ratio between the cold stream and hot CGM (background), $\mathcal{M}_b \equiv V_s / c_b$ is the stream velocity normalized by the CGM sound speed, $T_{s,4} \equiv T_s / (1.5 \times 10^4 \text{ K})$ is the stream temperature relative to thermal equilibrium with the UV background, $n_{s,0.01} \equiv n_s / (0.01 \text{ cm}^{-3})$ is the hydrogen number density in the stream, $\Lambda_{\text{mix},-22.5} \equiv \Lambda(T_{\text{mix}}, \rho_{\text{mix}}) / 10^{-22.5} \text{ erg s}^{-1} \text{ cm}^3$ is the net cooling rate in the turbulent mixing layer assumed to have temperature and density $T_{\text{mix}} = \delta^{1/2} T_s$ and $\rho_{\text{mix}} = \delta^{-1/2} \rho_s$. The factor $\alpha_{0.1}$ is a dimensionless number parameterizing the growth rate of KHI in the non-linear regime in the absence of cooling, which depends on $V_s / (c_s + c_b)$, where c_s and c_b are the sound speeds in the stream and in the CGM. It is in the range $\alpha_{0.1} \sim (0.5-2)$ (Padnos et al. 2018; Mandelker et al. 2019).

5.2 Stream properties and disruption by KHI

A key input for evaluating $R_s / R_{s,\text{crit}}$ and our analysis of stream disruption is an estimate of the range of properties for the cold streams as they enter the virial radius, which we discuss in some detail. The stream properties at given halo mass and redshift are derived from a model that assumes pressure confinement of the cold streams by the hot CGM (Mandelker et al. 2020b). According to this model, the stream-to-CGM density ratio is

$$\delta_{100} \simeq 2.3 M_{v,12}^{2/3} (1+z)_7 \frac{T_{b,v}}{T_{s,4}}, \quad (8)$$

where $T_{b,v} \equiv T_b / T_v$ is the temperature in the outer CGM normalized by the halo virial temperature. The stream density is

$$n_{s,0.01} \simeq 15 M_{v,12}^{2/3} (1+z)_7^4 f_{h,0.3} \frac{T_{b,v}}{T_{s,4}}. \quad (9)$$

Here, the mass of the hot CGM is assumed to be $f_h f_b M_v$ with $f_b \sim 0.17$ the universal baryon fraction and $f_h \equiv 0.3 f_{h,0.3}$ the mass fraction of baryons in the hot CGM. The hot gas density profile in the outer CGM is assumed to follow an NFW profile with a concentration of $c = 10$. Finally, the stream radius is estimated as

$$R_s \simeq 7 \text{ kpc } (1+z)_7^{-1} \left(\frac{f_{\text{acc},s} T_{s,4}}{\eta f_{h,0.3} T_{b,v}} \right)^{1/2}. \quad (10)$$

Here, $\eta \equiv V_s / V_v \sim 0.9 \mathcal{M}_b T_{b,v}^{1/2}$ is the stream velocity normalized by the halo virial velocity, also related to the stream Mach number \mathcal{M}_b . The factor $f_{\text{acc},s}$ represents the accretion rate onto the halo along a given filament normalized by the average baryonic accretion rate onto the halo (eq. 6) divided by three streams. Taken altogether, we have

$$\frac{R_s}{R_{s,\text{crit}}} \simeq 60 M_{v,12}^{-1/3} (1+z)_7^{3/2} \frac{f_{\text{acc},s}^{1/2} f_{h,0.3}^{1/2} \Lambda_{\text{mix},-22.5} T_{b,v}^{1/2}}{\eta^{3/2} \alpha_{0.1} T_{s,4}}. \quad (11)$$

In general, for stream disruption this ratio has to be smaller than unity.

The Hydrogen column density in the stream is given by $N_s \equiv n_s R_s$. Using eqs. (9) and (10), it can be expressed in terms of halo mass and redshift in units of 10^{21} cm^{-2} as

$$N_{s,21} \simeq 3.25 M_{v,12}^{2/3} (1+z)_7^3 \left(\frac{f_{\text{acc},s} f_{h,0.3} T_{b,v}}{\eta T_{s,4}} \right)^{1/2}. \quad (12)$$

When the stream is photo-heated by external radiation, N_s is monotonic with the optical depth, and $R_s / R_{s,\text{crit}}$ is correlated with N_s .

We see from eq. (11) that, for the fiducial case (where all the parameters as normalized in the equation are set to unity), streams are significantly larger than the critical radius for survival and growth. In fact, for fiducial streams, entrainment of hot CGM gas onto the cold stream can roughly triple the cold gas inflow rate onto the galaxy compared to the inflow onto the halo (Mandelker et al. 2020b; Aung et al. 2024). However, there is significant uncertainty in the various normalization parameters, and these can significantly lower $R_s / R_{s,\text{crit}}$. For example, the number of cosmic web filaments that connect to a halo (halo connectivity) is expected to be a function of the peak-height of the halo (Codis et al. 2018). Therefore, the number of filaments feeding a halo of a given mass can increase with redshift, such that it is reasonable to assume that six filaments or more feed a halo of $\sim 10^{12} M_\odot$ at $z \sim 6$ (Codis et al. 2018), which also seems consistent with cosmological simulations (e.g. Mandelker et al. 2021). This would naturally decrease $f_{\text{acc},s}$ by a factor of $\gtrsim 2$. Combined with reasonable scatter in the total accretion rate implies that $f_{\text{acc},s} \sim 0.25$ is reasonable. In post-FFB galaxies, where the stellar-to-halo mass ratio is high, the baryonic mass fraction in the hot CGM may be low, so $f_{h,0.3} \sim 0.5$ is reasonable. The CGM temperature near the virial shock is set by the shock jump conditions and is often less than T_v (Birnboim & Dekel 2003) which reflects the average temperature in a hydrostatic halo. Cosmological simulations also show that the CGM temperature in the outer halo is typically less than T_v (Lochhaas et al. 2021). Therefore, $T_{b,v} \sim 0.5$ is also reasonable. If the streams are heated either by local external sources of radiation from nearby galaxies or by internal turbulence, one could also reasonably obtain $T_{s,4} \sim 2$. Taking all of these together, we still

have $R_s/R_{s,\text{crit}} \sim 7 M_{v,12}^{-1/3} (1+z)_7^{3/2}$. If the streams enter the halo at the escape velocity rather than the virial velocity, then $\eta \sim 1.4$ and $R_s/R_{s,\text{crit}} \sim 2.5$. We thus find that even with assumptions that are favorable for stream disruption, streams at $z \gtrsim 6$ are still expected to be in the fast-cooling entrainment regime and thus hard to be disrupted by KHI.

At $z \sim 1-4$, the turnover in the observed star-forming main sequence, where the sSFR begins declining, is found to be well fit by the mass for which the fiducial $R_s/R_{s,\text{crit}} \sim 20$ rather than unity (Daddi et al. 2022a). This rather high threshold ratio could be explained by the fact that idealized shear-layer simulations suggest that when the ratio is $\lesssim 10$ the cold gas mass initially declines before eventually rising due to late onsetting entrainment (e.g. Gronke & Oh 2020a; Mandelker et al. 2020a; Kanjilal et al. 2021). Furthermore, supersonic velocities with $\mathcal{M}_b \gtrsim 2$ (as expected for streams in free-fall, Mandelker et al. 2020b; Aung et al. 2024) can suppress entrainment by a factor of $\gtrsim 2$ and lead to cold gas evaporation even in the nominal fast-cooling regime (Yang & Ji 2023). If correct, this implies that a ratio of $R_s/R_{s,\text{crit}} \sim 7$ may be small enough to initiate quenching. On the other hand, idealized simulations of cold streams flowing through a hot CGM in hydrostatic equilibrium within an NFW-halo potential show that even if $R_s/R_{s,\text{crit}} < 1$ at R_v , such that the cold gas mass declines initially due to KHI, the ratio increases as the stream flows down the potential well due to the larger ambient pressure, and there is always some radius $r < R_v$ where entrainment begins and the cold gas mass starts increasing (Aung et al. 2024). Furthermore, even weak self-gravity in the streams can reduce KHI-induced mixing due to buoyancy forces (Aung et al. 2019), while magnetic fields stabilize KHI by magnetic tension (Berlok & Pfrommer 2019), with each process extending stream lifetimes by factors of a few. These make the shutoff of feeding by streams more challenging.

5.3 Other disruption mechanisms

Other potential avenues of stream disruption besides KHI have been explored. For example, streams at $z \gtrsim 5$ are expected to be gravitationally unstable (Mandelker et al. 2018) in the sense that their mass-per-unit-length is greater than the maximal value for hydrostatic equilibrium (Ostriker 1964). In this case, the streams can fragment into gravitationally bound clumps prior to reaching the central galaxy, potentially leading to star formation and even globular cluster formation within the CGM (Mandelker et al. 2018; Aung et al. 2019). Certain cosmological simulations indeed show star formation in streams in a manner consistent with this model (Mandelker et al. 2018; Bennett & Sijacki 2020), though it is unclear how reliable these results are given the limited resolution in the CGM and the very crude star-formation recipes used in the simulations. Even if this were the case, it is unclear why this would lead to complete galaxy quenching, since the cold gas in the streams would still contribute to star formation even if outside the central galaxy.

Another possibility is that the gas in intergalactic cosmic web filaments is heated up by a cylindrical accretion shock to virial temperatures of $\sim 10^6\text{K}$ prior to entering the halo virial radius. This is expected to occur in cosmic web filaments above a critical line-mass (Lu et al. 2024), in much the same way as the CGM in halos above a critical mass is expected

to be hot (Dekel & Birnboim 2006). However, preliminary estimates suggest that while filaments feeding halos of $M_v \sim 10^{12} M_\odot$ at $z > 4$ indeed support a stable accretion shock at the cylindrical virial radius of the dark matter filament (referred to as a hot circum-filamentary medium, or CFM), the filaments still harbor a significant cold gas fraction in their centers due to the cooling time being only slightly longer than the free-fall time (Lu et al. 2024; Aung et al. 2024). It thus seems unlikely that the cold gas supply onto such halos can be completely shut off by cylindrical virial shocks in cosmic web filaments.

Finally, it has been speculated that the cold gas streams at the centers of hot cosmic-web filaments may “shatter” when penetrating the virial shock around massive halos. This is because the confining pressure in the hot CGM is more than an order of magnitude larger than the confining pressure in the hot CFM (Lu et al. 2024; Yao et al. 2025). This can lead to a shock penetrating the cold stream radially (in a cylindrical sense) which then causes the stream to fragment into small cloudlets of size $l_{\text{cool}} \sim \min(c_s t_{\text{cool}}) \sim 10\text{pc}$ due to Richtmyer-Meshkov and thermal instabilities (McCourt et al. 2018; Gronke & Oh 2020a; Yao et al. 2025). These small cold clouds then disperse in the outer CGM and can be disrupted by hydrodynamic instabilities as they are smaller than the critical size for cloud survival (Gronke & Oh 2018, 2020b; Gronke et al. 2022). However, preliminary results testing this hypothesis in idealized simulations suggests that this does not shut off the flux of cold gas towards the central galaxy. This is because the rapid cooling of high density gas in the inner halo leads to strong coagulation of the resulting cloudlets, while the strong shear between the initial stream and the hot CGM focuses the coagulated gas into a (possibly more clumpy) stream-like structure (Yao et al., in prep.). Based on the aforementioned studies, we estimate that the critical stream radius above which coagulation will dominate over shattering is roughly a factor of ~ 2 larger than the critical radius above which entrainment dominates over mixing (eq. 7). As discussed above, typical streams are expected to be significantly larger than this (eq. 11), limiting shattering as a viable mechanism for stream disruption.

Two more promising avenues for stream disruption have yet to be considered in detail, both of which may be enhanced by strong AGN feedback. These are stream disruption by strong turbulence in the CGM and photo-heating of the streams by AGN radiation. Recall that AGN feedback is understood to operate in two different modes depending on the black-hole accretion rate. The thermal (or quasar) mode is dominant when the BH growth rate exceeds 1% of the Eddington limit, while the jet (or kinetic) mode operates at lower accretion rates (Heckman & Best 2014). The thermal mode may be particularly relevant during the early stages of quenching, as it is initiated by compaction or merger events which can trigger large gas inflow rates towards the center of the galaxy. As the quenching proceeds and the BH accretion rate drops below the 1% Eddington threshold, the AGN is assumed to transition to the kinetic (or jet) mode. In this regime AGN outflows, including jets and the associated winds, can inject turbulence into the CGM which could suppress the cold inflows as we see below. This may be particularly relevant in the denser inner regions of the halo, where the enhanced coupling between the outflows and the ambient gas may more effectively disrupt the cold streams in the turbulent environment.

Model	η	$f_{\text{acc},s}$	$f_{\text{h},0.3}$	$T_{s,4}$	$T_{\text{b},v}$	δ_{100}	$n_{s,0.01}$	$R_{s,1}$	$R_s/R_{s,\text{crit}}$	$N_{s,21}$
<i>fiducial</i>	1	1	1	1	1	2.3	15	7	60	3.2
<i>slow cooling</i>	$\sqrt{2}$	0.1	0.3	2	0.4	0.45	0.9	7.6	1.16	0.2
<i>fast cooling</i>	1	2	2	0.5	1	4.6	60	5	240	9.3
<i>low gas</i>	1	0.1	0.4	1	1	2.3	6	3.5	12	0.65

Table 1. Stream models. Listed are the normalization parameters and the corresponding stream properties based on the Mandelker et al. (2020b) model (eq. 8 to eq. 12), for a halo with $M_{v,12} = 1$ and $(1+z)_7 = 1$. In the *fiducial* model all the parameters are at their fiducial values. The *slow cooling* and *fast cooling* models minimize and maximize $R_s/R_{s,\text{crit}}$, thus maximize and minimize the chances for stream disruption, respectively. The *low gas* has small N_s and R_s that increase the stream survival, by reducing $f_{\text{acc},s}$ and f_{h} . In all models $\alpha_{0.1} = 1$ and $\Lambda_{\text{mix},-22.5} = 1$ (with no AGN).

5.4 Stream disruption by CGM turbulence

The first promising mechanism for stream disruption is due to a highly turbulent CGM, with turbulent Mach numbers \mathcal{M}_t of order unity or slightly higher with respect to the hot gas. Such turbulence may disrupt streams by generating shocks at the stream interface, potentially enhancing shattering, and also reducing the efficiency of entrainment.

A crude estimate for the disruptive effect of CGM turbulence on a stream can be obtained based on the analysis of Gronke et al. (2022) of cold clouds that are embedded in a hot turbulent medium. They find that the clouds disrupt once they are smaller than a critical size for survival, which increases rapidly with turbulent Mach number for supersonic turbulence. As shown in eq. 9 of Gronke et al. (2022), the survival criterion of clouds in a turbulent box was calibrated similarly to the classical cloud-crushing framework in a wind tunnel, but modified with an additional Mach number dependence. Specifically, the critical size for survival can be approximated as

$$R_{\text{turb}} \sim 10^{0.6\mathcal{M}_t} R_{\text{crit},w}, \quad (13)$$

where $R_{\text{crit},w}$ denotes the critical radius for cloud survival in a wind-tunnel setup, as defined in eq. 2 of Gronke et al. (2022). This wind-based criterion arises from equating the mixing-layer cooling timescale with the cloud-crushing timescale, and is analogous to the corresponding radius for streams (eq. 7) which was calibrated by equating the mixing-layer cooling timescale with the KHI mixing timescale. For clouds, the Mach number \mathcal{M} in the expression for the wind $R_{\text{crit},w}$ is replaced by the turbulent Mach number \mathcal{M}_t , reflecting the enhanced mixing and dynamical disruption driven by turbulence compared to a laminar wind. This is sensible for a spherical cloud where much mixing occurs behind the bow shock near the cloud head in wind-tunnel setups (Kaul et al. 2025), and is therefore likely to similarly arise behind turbulent shocks distributed isotropically. However, for streams, the primary mixing and disruption mechanism is KHI induced by the bulk flow rather than a bow shock or something similar (Mandelker et al. 2020a; Kaul et al. 2025). Therefore, we speculate as an educated guess based on previous results that the Mach number \mathcal{M} in the expression for the wind $R_{\text{crit},w}$ should remain the bulk Mach number as in eq. (7), with the turbulent critical radius given by eq. (13), namely multiplying $R_{\text{crit},w}$ by $10^{0.6\mathcal{M}_t}$. For $\mathcal{M}_t = 1$, this will lower $R_s/R_{s,\text{crit}}$ by a factor of ~ 4 with respect to eq. (11). We stress that this increased survival radius due to turbulence is in addition to the aforementioned reduced entrainment efficiency for supersonic flows based on Yang & Ji (2023), with the relation between them not yet clear. This may also help explain the observed association of the thresh-

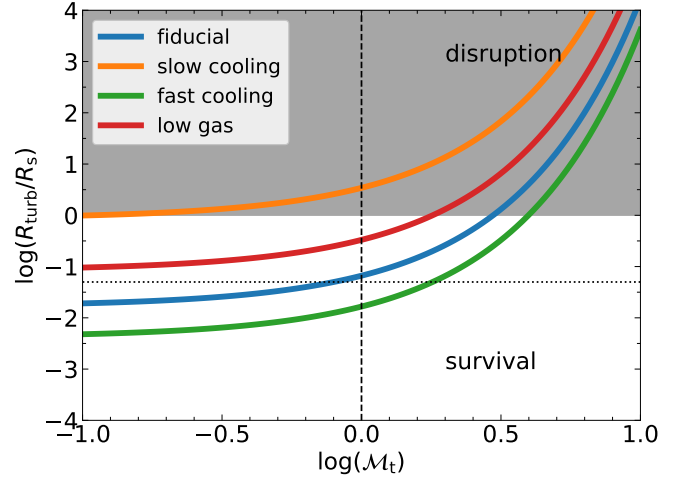


Figure 5. Stream disruption by CGM turbulence. Shown is an estimate of the critical stream radius for disruption by CGM turbulence, with respect to the actual stream radius as a function of the turbulent Mach number (where the transonic point is marked by a vertical dashed line). This estimate is based on a crude extrapolation of the results for clouds (Gronke et al. 2022) to streams. The cases shown refer to stream properties in $M_v \sim 10^{12} M_\odot$ halos during the central phase of the post-FFB quiescent regime at cosmic morning, $z \sim 6$. The relevant parameters of the four cases are listed in Table 1. We learn that, with respect to $R_{\text{turb}}/R_s = 1$ (the horizontal line separating the shaded and un-shaded areas), the *slow cooling* stream is expected to be capable of being disrupted even by subsonic turbulence. The *low gas* stream may disrupt even by transonic or slightly supersonic turbulence. On the other hand, the *fiducial* stream and the *fast cooling* stream seem to require supersonic turbulence of $\mathcal{M}_t \sim 3$ for disruption. With respect to the threshold $R_{\text{turb}}/R_s = 0.05$ (which is motivated by observations - the horizontal dotted line), the fiducial streams are expected to be disrupted even by transonic turbulence.

old $R_s/R_{s,\text{crit}} \sim 20$ with the turnover of the star-forming main sequence (Daddi et al. 2022b).

The stream disruption is evaluated for four different models of stream properties, presented in Table 1. They are based on the Mandelker et al. (2020b) model (eq. 8 to eq. 12, for a halo with mass $M_v = 10^{12} M_\odot$ at $z = 6$). In these models the normalization parameters in eq. (11) are varied, to minimize or maximize $R_s/R_{s,\text{crit}}$, thus spanning a *fiducial* case along with streams more prone to disruption and streams more prone to survival. In the *fiducial* model all the normalization parameters are at their fiducial values. The *slow cooling* model chooses parameters in order to minimize the ratio of $R_s/R_{s,\text{crit}}$ thus maximizing the chances for stream disruption. The *fast cooling* model chooses parameters in order to maximize $R_s/R_{s,\text{crit}}$ and thus maximize the chances for stream survival and growth. The *low gas* model chooses parameters to have a small N_s and R_s by reducing the accretion factor per

stream $f_{\text{acc},s}$ and the fraction of baryons in the hot CGM f_h . In all models we keep $\alpha_{0.1} = 1$ and $\Lambda_{\text{mix},-22.5} = 1$ (with no AGN). While each of these can provide an extra factor of two in $R_s/R_{s,\text{crit}}$ independent of AGN, they have no effect on the physical properties such as δ , n_s , R_s and N_s . The correlation of $R_s/R_{s,\text{crit}}$ and N_s indicates that streams with slow/fast cooling, which are easier/harder to disrupt by KHI, are also more/less susceptible to heating by AGN.

Figure 5 shows the estimated critical stream radius for disruption by turbulence with respect to the stream radius, R_{turb}/R_s , as a function of the turbulent Mach number \mathcal{M}_t , based on eq. (11) and eq. (13). While all four cases of stream properties seem to be in the survival regime based on the fact that $R_s/R_{s,\text{crit}}$ is larger than unity according to eq. (11), Fig. 5 shows that they are all pushed into the disruption regime when \mathcal{M}_t is sufficiently large. If one considers the observationally motivated threshold of ~ 0.05 rather than ~ 1 , this is made even more pronounced. We comment that due to the steep increase of R_{turb} with Mach number in the supersonic regime, the threshold Mach number for stream disruption is only weakly dependent on redshift and halo mass. While sustaining significant turbulence in the outer CGM would probably require intense accretion or mergers, stream disruption may be more feasible in the inner CGM, where the supersonic fraction can be substantial, driven by the interplay between cooling flows and feedback processes.

A specific scenario for a turbulent CGM has been proposed by Stern et al. (private communication) based on spherical simulations and cosmological FIRE simulations. Following the results for cold inflow in halos of $M_v \leq 10^{11} M_\odot$ and for hot halos when $M_v \geq 10^{12} M_\odot$ (Birnboim & Dekel 2003; Kereš et al. 2005; Dekel & Birnboim 2006; Kereš et al. 2009), they find that halos of intermediate mass, $M_v \sim 10^{11.5} M_\odot$, develop a cold, turbulent inner region that may aid in disrupting the stream. The turbulence may be driven either by the inflowing streams themselves, by contracting cooling flows in the CGM, or by mergers through compaction events. AGN feedback from the galaxy (not included in these simulations) may increase the turbulence to even higher levels than inferred in the simulations and/or push it up to higher halo masses. However, the CGM in this scenario, as studied at low redshifts, is relatively cold, with temperatures $T \sim (2 \times 10^5) \text{K}$. It is unclear how to extrapolate their results to high redshifts and whether it would be consistent with the assumption of Mandelker et al. (2020b), which is the basis for our current model, that the CGM is hot and in pressure equilibrium with the cold stream.

Several caveats are worth noting regarding the speculative crude extrapolation from clouds to streams. First, the steep increase in R_{turb} with supersonic Mach number warrants further exploration since Gronke et al. (2022) calibrated their parameters primarily in the subsonic regime. Second, if the clouds are much larger than the minimal size for cloud survival or the turbulence is subsonic or transonic, the cloud growth can actually be enhanced by entrainment (Gronke et al. 2022). We thus caution that the net effect of CGM turbulence on realistic streams is yet to be investigated more accurately using simulations (Yao et al., in prep.).

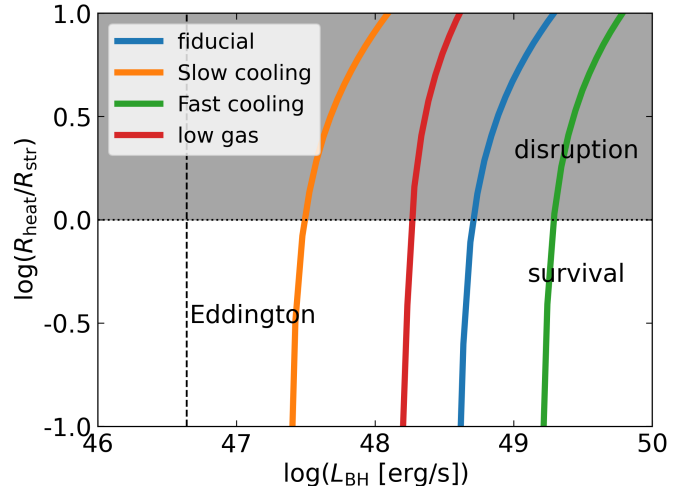


Figure 6. Direct photo-heating of a cold stream by an AGN. Shown is the depth into the stream where the equilibrium temperature has increased to above 10^5K , R_{heat} , with respect to the stream radius R_s , as a function of AGN luminosity L_{bh} . The different cases of stream properties are listed in Table 1 for a $10^{12} M_\odot$ halo at $z \sim 6$. The metallicity in the stream is assumed to be $0.03 Z_\odot$. The vertical line refers to the Eddington luminosity $L_{\text{bh}} = 4 \times 10^{46} \text{erg s}^{-1}$ for a central black hole of mass $M_{\text{bh}} = 10^{8.5} M_\odot$. We learn that the disruption of streams by direct heating requires bursts with luminosities significantly higher than the Eddington luminosity.

5.5 Stream disruption by photo-heating from AGN

The second way by which AGN can potentially disrupt streams even more directly is by radiative heating. High resolution cosmological simulations with explicit radiative transfer have shown that in dwarf galaxies ($M_v \lesssim 10^8 M_\odot$) during the epoch of reionization ($z > 6$), photo-heating from starbursts in the central galaxies can heat the gas in the cosmic web filaments feeding these galaxies to temperatures of $T \gtrsim 10^{4.5} \text{K}$ (Katz et al. 2020). Since the filaments feeding these low-mass halos have virial temperatures of $\lesssim 10^4 \text{K}$, this prevents gas from cooling to the center of the dark matter filament and forming the cold stream which otherwise would have fed the central galaxy. It can even totally unbind the filament gas, thus effectively shutting off the cold gas supply to the central galaxy. This process is similar to so-called ‘reionization feedback’ in low mass halos with $T_v \lesssim 10^4$, which is thought to be the primary reason that such low-mass halos remain dark with no appreciable star formation over cosmic history (e.g. Benitez-Llambay & Frenk 2020). The filaments that feed the massive quiescent galaxies during cosmic morning have virial temperatures of $\sim (10^{5.5} - 10^6) \text{K}$ (Lu et al. 2024; Aung et al. 2024), and as such will likely not be affected by photoheating from central star formation. However, AGN heating may heat the gas to much higher temperatures, in excess of 10^5K and perhaps even 10^6K , which would have similar suppression effects on the cold streams feeding these massive galaxies.

The massive quiescent galaxies observed at cosmic morning are typically of stellar mass $\sim 10^{10.5} M_\odot$, suggesting central black holes of $\sim 10^{8.5} M_\odot$ assuming a high BH-to-stellar mass ratio of ~ 0.01 (Harikane et al. 2023b; Maiolino et al. 2024). The corresponding Eddington luminosity is $L_{\text{edd}} \simeq 4 \times 10^{46} \text{erg s}^{-1}$.

5.5.1 Direct heating of the streams

Motivated by these estimates, we consider how the radiation from a central AGN with a given luminosity L_{bh} might directly heat an inflowing cold stream of gas number density n_s and metallicity Z . We consider a stream with orbital angular momentum about the central galaxy and an associated impact parameter, such that in practice it is irradiated from the sides. We ignore absorption outside the stream, and assume absorption by the stream gas as it is photoionized and photo-heated by the radiation to an equilibrium temperature T_{eq} . The radiation flux at a distance r from the AGN and a penetration depth x into the stream is computed by

$$F_{\text{bh}}(r) = \frac{L_{\text{bh}}}{4\pi r^2} e^{-\tau(x)}, \quad (14)$$

where

$$\tau(x) = \int_0^x n_s \sigma dx, \quad (15)$$

with σ the cross section for absorption. We assume thermal equilibrium of the stream gas under photoionization and collisional ionization, and use Cloudy (Ferland et al. 2017) to compute σ (using L_{bh} and Z), and the temperature distribution $T_{\text{eq}}(r)$ (using L_{bh} and n_s). We define the heating penetration depth R_{heat} as the penetration distance x within the stream where T_{eq} exceeds 10^5K . Even though this may be below the virial temperature of the dark matter filament, such that the gas does not become fully unbound, gas at temperatures $\sim 10^5\text{K}$ would be more vulnerable to disruption by turbulence, quasar winds, or hydrodynamic instabilities, making it easier for AGN to suppress cold stream accretion. This can be qualitatively understood by considering $T_{s,4} \gtrsim 10$ in eqs. (8) to (12).

For an isothermal stream embedded in an isothermal halo, the cold stream gas density approximately follows $n_s \propto r^{-2}$ (Mandelker et al. 2018, 2020b)¹. The radiation flux likewise decays as $F \propto r^{-2}$. Since the equilibrium temperature is largely determined by the ionization parameter that is proportional to F/n , it is not expected to change much with galactocentric radius. This implies that our evaluation of the photoheating can serve as a crude approximation at any r within R_v .

As before, we adopt the stream parameters listed in Table 1 based on the analytic model of Mandelker et al. (2020b). Figure 6 shows the heating penetration depth R_{heat} with respect to the stream radius R_s as a function of AGN luminosity L_{bh} for the different models of stream properties. The Eddington luminosity is marked at $L_{\text{edd}} \simeq 4 \times 10^{46} \text{ erg s}^{-1}$ assuming a black-hole of mass $\sim 10^{8.5} M_{\odot}$. We learn that, even for the *slow cooling* model, a luminosity of a few Eddington luminosities is required for direct heating and disruption of the streams. Given the observational indications that about one third of the massive black holes at cosmic morning may exceed the Eddington luminosity (Trakhtenbrot et al. 2011; Farina et al. 2022), we conclude that intermittent super-Eddington AGN outbursts could possibly heat the inflowing cold streams, if they are in the slow cooling regime. The fiducial streams would require a luminosity higher than $L_{\text{bh}} \sim 10^{48} \text{ erg s}^{-1}$, which is less likely.

¹ For an NFW halo in hydrostatic equilibrium the density profile is even steeper (Aung et al. 2024).

The above analysis is very preliminary and should be taken with a grain of salt. In particular, absorption in the stream should be more carefully accounted for, along with scattering and re-emission as well as the effects of ionization by the UV background versus self-shielding (Mandelker et al. 2018; Aung et al. 2024). These effects might make the overall heating even weaker, because more radiation might be absorbed in the outer shell, thus enhancing the shielding of the inner core. Second, the claimed invariance to the distance from the AGN along the stream, given the higher density and higher flux at smaller radii, should be considered more carefully to account for realistic stream and halo which are not necessary isothermal, with profiles steeper than $n_s \propto r^{-2}$ (Aung et al. 2024). Properly accounting for these effects will require detailed modeling using semi-analytic radiative transfer methods or full simulations.

5.5.2 Indirect disruption by slow cooling in the mixing layer

While we found that streams in the high-density range are not likely to be disrupted by direct AGN heating, the AGN radiation may make the streams more prone to disruption by KHI. This is by increasing the cooling time of gas within the turbulent mixing layers between the cold streams and the hot CGM such that it exceeds the shear timescale. Under such conditions, the entrainment of hot gas into the cold stream is ineffective, allowing KHI to disrupt the streams, similar to the case with no cooling analyzed in Mandelker et al. (2019). In practice, this manifests as decreasing the parameter $\Lambda_{\text{mix},-22.5}$ in eq. (11) due to AGN photo-heating in the mixing layer, increasing T_{mix} and the stream temperature, while decreasing n_{mix} and the stream density, and changing the ionization state of the mixing layer by AGN photoionization.

Figure 7 shows the Λ curves of net heating minus cooling as a function of temperature for different AGN luminosities, L_{bh} , including the case of no AGN. Only the *fiducial* stream model from Table 1 is shown as an example. The cooling curves are derived at constant pressure, meaning assuming that the gas density scales as $n \propto T^{-1}$, with the normalization set by the stream value in each model. The cooling function Λ is computed for the given gas density and temperature and the given AGN radiation intensity in the mixing layer between the cold stream and the CGM at the virial radius, over the temperature range from the stream edge ($\sim 10^4\text{K}$) to the CGM temperature. The symbols in Fig. 7 mark the point on each curve where $T = (T_{\text{eq}} T_{\text{max}})^{1/2}$, where T_{eq} is the lowest temperature where $\Lambda = 0$ and T_{max} is either T_{CGM} or $2 \times 10^7\text{K}$ if there is net cooling or net heating at T_{CGM} , respectively. As L_{bh} increases, so does the temperature where the outer edge of the stream is in thermal equilibrium. With no AGN, this is set by thermal equilibrium with the UV background at $T_{\text{eq}} \sim (1-3) \times 10^4\text{K}$ depending on the stream density. AGN increase T_{eq} by providing extra heating. At L_{Edd} , T_{eq} is ~ 5 times higher, while at $10 L_{\text{Edd}}$ it can be as high as $\sim 10^7\text{K}$.

Figure 8 shows T_{eq} as a function of L_{bh} for our four stream models from Table 1. The curves show T_{eq} assuming isobaric (constant pressure) heating and cooling as discussed above. The equilibrium temperature gradually increases with L_{bh} from $\sim (2-3) \times 10^4\text{K}$ at $L_{\text{bh}} = 0.01 L_{\text{Edd}}$ to $\sim 10^5\text{K}$ at $L_{\text{bh}} \sim (1-10)L_{\text{Edd}}$ before rapidly increasing to $\sim 10^7\text{K}$.

This increase in T_{eq} with increasing L_{bh} leads to a corre-

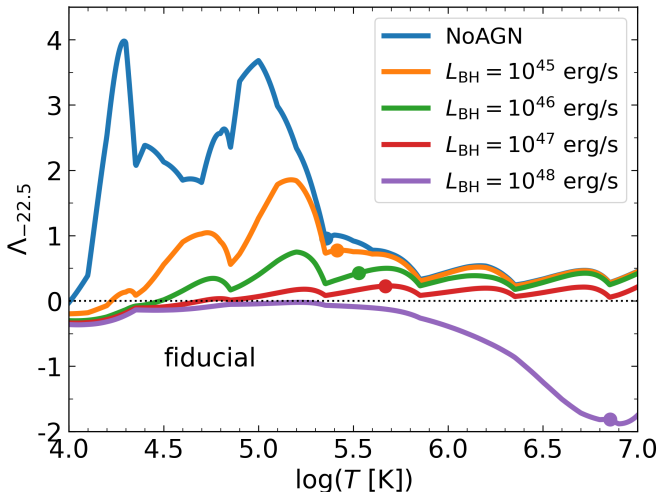


Figure 7. Indirect disruption of a cold stream by an AGN. Shown is the net cooling minus heating rate, $\Lambda_{-22.5} = \Lambda(T)/10^{-22.5} \text{ erg s}^{-1} \text{ cm}^3$, as a function of temperature for different values of AGN luminosity L_{bh} including no AGN (blue lines). It is shown as an example for the *fiducial* model for stream properties from Table 1. The cooling curves are computed assuming constant pressure, $nT = n_s T_s$. The horizontal dotted line marks thermal equilibrium, where the net cooling is zero. Above (below) this line, the system is undergoing net cooling (heating). The circles on each curve show the mixing temperature, $T_{\text{mix}} = (T_{\text{eq}} T_{\text{CGM}})^{1/2}$, with T_{eq} the lowest temperature where $\Lambda_{-22.5} = 0$. As the AGN luminosity increases, T_{eq} increases while $\Lambda_{\text{mix}} = \Lambda(T_{\text{mix}})$ decreases, by up to an order of magnitude for $L_{\text{bh}} \sim L_{\text{Edd}}$. This implies that the stream and the mixing layer contain much warmer, more diffuse gas than without the AGN, and suggests that the streams are much more prone to disruption.

responding increase in the mixing temperature, which we now define as $T_{\text{mix}} = (T_{\text{eq}} T_{\text{CGM}})^{1/2}$, generalizing our earlier definition of $(T_s T_{\text{CGM}})^{1/2}$. For most cases, we leave the density and temperature in the CGM unchanged from Table 1. However, if the cooling curve shows net heating at T_{CGM} for given stream model and L_{AGN} , we set $T_{\text{CGM}} = 10^7 \text{ K}$ and determine the density by enforcing constant pressure. For each curve in Fig. 7, T_{mix} is marked with a circle. For all models, $\Lambda_{\text{mix}} = \Lambda(T_{\text{mix}}) \sim 10^{-22.5} \text{ erg s}^{-1} \text{ cm}^3$ without AGN, and is $\gtrsim 10$ times smaller at L_{Edd} . At $10 L_{\text{Edd}}$, the entire mixing layer and even the CGM itself may undergo net heating.

Figure 9 shows $R_s/R_{s,\text{crit}}$ as a function of L_{bh} following eq. (11) with Λ_{mix} computed as described above. The decline in Λ_{mix} causes a corresponding decline in $R_s/R_{s,\text{crit}}$. Our *slow cooling* stream model enters the disruption regime, with $R_s/R_{s,\text{crit}} < 1$, at very low AGN luminosities of $\gtrsim 0.01 L_{\text{Edd}}$. The *low gas* and *fiducial* models enter this regime at $\sim 3 L_{\text{Edd}}$ and $9 L_{\text{Edd}}$ respectively. However, they fall below the empirically motivated threshold of $R_s/R_{s,\text{crit}} < 20$ at sub-Eddington luminosities, suggesting that they will be more prone to disruption. The inclusion of turbulence in this slow-cooling regime would make the stream disruption even more effective. On the other hand, our *fast cooling* stream model remains above even this more-lenient threshold at least until $\sim 40 L_{\text{Edd}}$ and is likely to survive.

5.6 Quenching by disk turbulence

If the streams do manage to penetrate through the CGM into the central disk, they provide gas supply for star formation, but they also drive turbulence in the disk that may suppress the

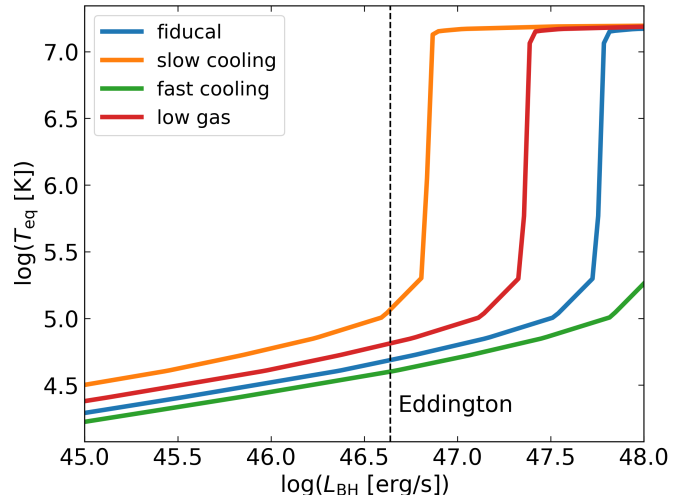


Figure 8. Indirect disruption of a cold stream by an AGN. Shown is the equilibrium temperature, T_{eq} , as a function of AGN luminosity, L_{bh} , based on the cooling curves shown in Fig. 7. This is the lowest temperature where the net cooling minus heating vanishes and the gas is in thermal equilibrium. As such, this represents the temperature to which the outer layer of the stream will heat in the presence of an AGN from its initial equilibrium temperature of $T_{\text{eq}} \sim (1-3) \times 10^4 \text{ K}$ when exposed only to the UV background. When the gas evolves at constant pressure, then T_{eq} gradually rises to $\sim 10^5 \text{ K}$ at $\sim (1-10) L_{\text{Edd}}$ followed by a very rapid rise to $\sim 10^7 \text{ K}$. (If the gas evolves at constant density this rapid increase is absent, and the stream rarely reaches $T_{\text{eq}} > 10^5 \text{ K}$.)

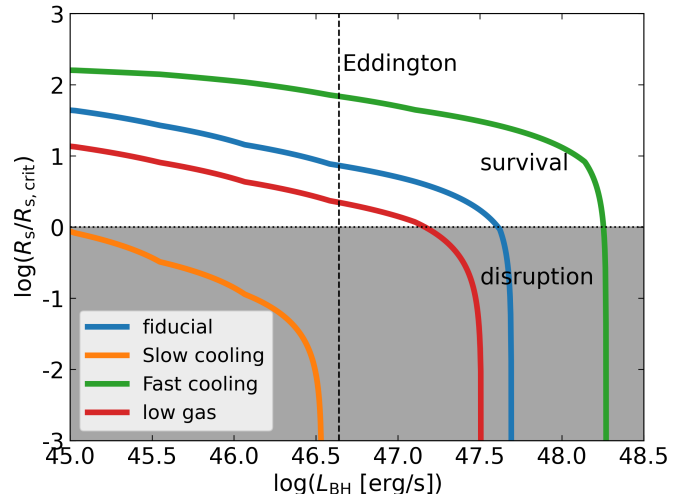


Figure 9. Indirect disruption of a cold stream by an AGN. Shown is the ratio of the stream radius to the critical value for disruption by KHI (eq. 11) as a function of L_{bh} for our different stream models from Table 1. As L_{bh} increases, $\Lambda_{\text{mix},-22.5}$ from eq. (11) decreases (Fig. 7), while the rest of the parameters remain fixed. Model *slow cooling* reaches $R_s/R_{s,\text{crit}} < 1$ at $L_{\text{bh}} \sim 0.01 L_{\text{Edd}}$, implying rapid disruption. While the *low gas* and *fiducial* models only enter this regime at $\sim (10-20) L_{\text{Edd}}$, they fall below the empirically motivated threshold of $R_s/R_{s,\text{crit}} < 20$ at sub-Eddington luminosities, suggesting they will be more prone to disruption. The *fast cooling* model stays above this higher threshold until $L_{\text{bh}} \gtrsim 30 L_{\text{Edd}}$, suggesting it is likely to survive the presence of strong AGN.

disk instability and thus slow down star formation. Gabor & Bournaud (2014), using analytic modeling and isolated-disk simulations, showed that the streams are indeed expected to be effective in suppressing star formation this way at $z > 2-3$. This is consistent with the finding of Ginzburg et al. (2022) that at $z > 3$ the driving of disk turbulence is dominated by the incoming streams over stellar feedback and instability-driven radial transport in the disk. However, the preliminary estimates provide suppression of SFR by a factor of only a few, which may not be enough for the complete quenching required. Furthermore, the efficiency of this suppression in post-FFB galaxies versus non-FFB galaxies is yet to be verified. One should also recall that the turbulence may in turn enhance the SFR by generating giant clumps due to excessive compressive modes of turbulence (Inoue et al. 2016; Mandelker et al. 2025; Ginzburg et al. 2025). More elaborate and accurate simulations are required in order to properly investigate this potential SFR suppression mechanism.

6 POST-FFB QUENCHING

6.1 FFB contribution to quenching

Considering the quenching mechanisms discussed above, one wishes to identify the ways by which the FFB phase promotes the strong post-FFB quenching, in comparison to the supposedly weaker quenching in galaxies that did not undergo an FFB phase. In general, given that the FFB evolutionary tracks consist of halos that are more massive than the halos on the non-FFB tracks, they cross the quenching thresholds earlier, and at any given time they find themselves higher above the thresholds, thus obeying the quenching conditions in a stronger way.

A key argument for post-FFB quenching is that compaction events are more likely in high-sigma peaks. Simulations (Dubois et al. 2012; Codis et al. 2012) show that the rare massive halos at high redshifts are largely fed by low-AM streams into compact bulges, with specific AM an order of magnitude smaller than that of the baryons in the halo. These streams penetrate deep inside the halo and connect to the bulge from multiple rapidly changing directions. This causes enhanced cancellation of AM in rarer halos, fed by more isotropically distributed streams. A complementary effect that enhances compaction events in the FFB halos emerges from the fact the high-sigma peaks tend to be clustered (Bardeen et al. 1986). This induces a higher than average rate of galaxy collisions, mergers, and the associated compaction events, which cause quenching in multiple ways as described above. However, this effect is expected to be rather weak.

A highly distinctive feature of post-FFB galaxies is the boost in BH growth by rapid core collapse in the young, rotating star clusters and the subsequent inspiral in galactic disks to initial SMBH growth by mergers (Dekel et al. 2025). The massive BH formed by mergers can eventually lead to enhanced accretion and AGN activity that may provide the crucial quenching mechanism, including the driving of CGM turbulence which may stop the gas supply by streams.

Another source for the abrupt onset of quenching is the gas depletion from the inter-stellar medium (ISM) during the FFB phase. Then, in the absence of such local gas reservoir, quick

quenching can be achieved solely by stopping the external gas supply.

6.2 Peak of galaxy formation at cosmic noon

Along the non-FFB evolutionary track, the highly abundant 2σ -peak halos reach the upper region of the golden mass, $\sim 10^{12} M_{\odot}$, at cosmic noon. In such halos the CGM is hot, fed both by feedback-driven outflows from the galaxy and virial-shock-heated inflow inside the halo virial radius. This allows the cold streams to be intensified by entrainment of the hot gas, thus utilizing recycled gas for increased SFR beyond the accretion rate of baryons onto the halo (Aung et al. 2024).

As lower-sigma peaks than halos on the FFB track, the non-FFB halos are fed by streams with higher AM, which translates to fewer compaction events and less of the associated quenching that they induce. These halos are also less clustered and tend to suffer less galaxy interactions and mergers, thus producing less compaction events.

7 OBSERVABLE PREDICTIONS

7.1 Bimodality in morphology at cosmic dawn

There are observational indications for a wide range of galaxy sizes among the high-redshift excessively bright galaxies, especially at $z \geq 10$. Harikane et al. (2025) refer to this as a bimodality in morphology, between compact galaxies on one hand and extended, clumpy galaxies on the other hand. The actual division to two distinct types is yet to be confirmed as it is based on a small number of galaxies, but there is clearly large variety in size and clumpiness. Ono et al. (2025), who investigating 169 galaxies at $z \sim 10-16$, find a log-normal distribution of effective radii with a mean of $R_e \sim 133$ pc and standard deviation $\sigma_{\ln R_e} \sim 0.015$, the latter being comparable to disks at low redshifts. They identify only two extremely compact galaxies with $R_e \sim 30-60$ pc.

Our ongoing zoom-in cosmological simulations (Andalman et al. 2024, Yao et al., in preparation, Chen et al., in preparation) indicate that a given galaxy may evolve from a compact configuration at one time to an extended configuration at another time, and vice versa (see also simulations by Ono et al. 2025). The extended configuration tends to be associated with mergers, which in these simulations are mostly minor mergers between galaxies that are dominated by gas. The extended configuration could be due to capturing the incoming merging galaxies within the primary halo prior to the first pericenter passage or later near turnaround at the following apocenter prior to the final coalescence. Alternatively it could be due to post-merger expansion as a result of energy gain during the merger, including outflows and star formation in the outskirts. This is being investigated elsewhere (Yao et al., in preparation).

One may alternatively envision that the range of morphologies of the star forming galaxies at cosmic dawn is associated with the bimodality discussed in the current paper between galaxies on the FFB and the non-FFB evolutionary tracks (§2). The FFB galaxies that are associated with high-sigma peaks tend to be fed by streams of lower angular momentum (Dubois et al. 2012) and thus lead to more compact galaxies, while the lower-sigma, non-FFB galaxies tend to be fed

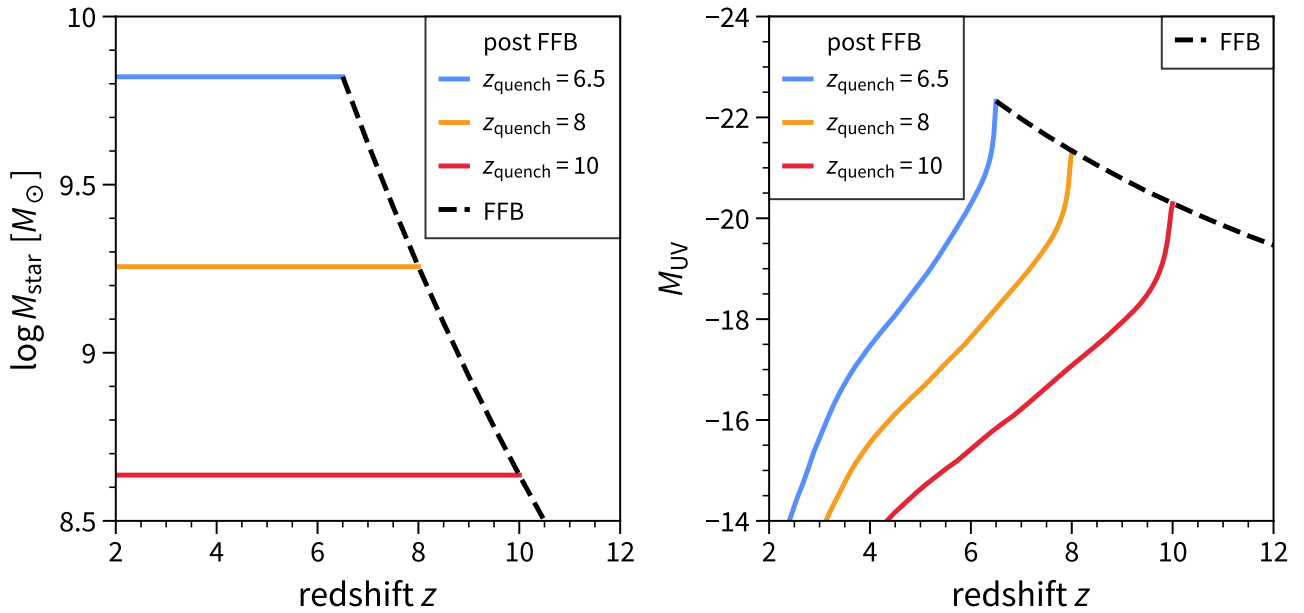


Figure 10. The predicted stellar mass and UV magnitude of galaxies on the fiducial FFB evolutionary track as a function of redshift of observation. The onset of quenching is assumed to be at $z=6.5, 8, 10$ (blue, orange, red), with the FFB and quiescent phases marked by dashed and solid lines respectively. The growth in time at high z reflects the star formation in the FFB phase. The decline of brightness in time after the onset of quenching is due to passive evolution at the post-FFB quiescent phase.

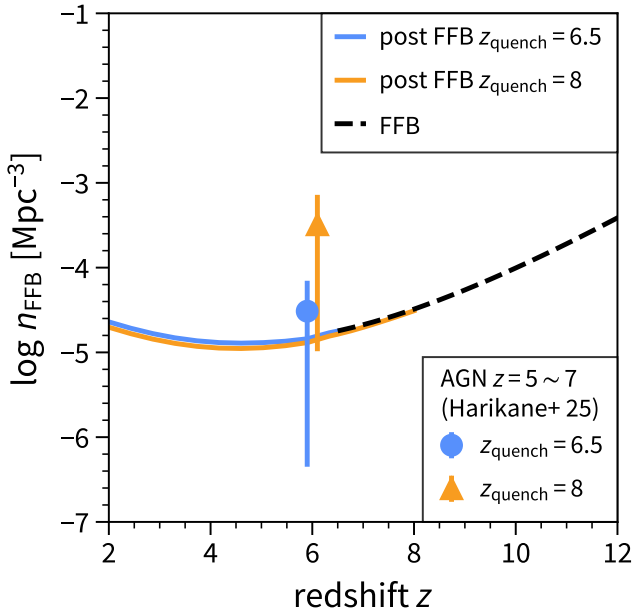


Figure 11. The predicted comoving number density of galaxies on the FFB and post-FFB evolutionary track, including the galaxies brighter than the fiducial FFB galaxies, as a function of redshift at cosmic dawn and cosmic morning. The onset of quenching is assumed to be at $z_{\text{quench}}=8$ (orange) and $z_{\text{quench}}=6.5$ (blue), with the FFB and quiescent phases marked by dashed and solid lines respectively. We learn that the predicted number density of post-FFB quiescent galaxies at $z \sim 6$ is $n \gtrsim 10^{-5} \text{ Mpc}^{-3}$. Shown for comparison are number densities of AGN observed by JWST (Harikane et al. 2023b) at $z=5-7$ in quiescent galaxies brighter than the corresponding predicted UV magnitude predicted in Fig. 10. The abundance of BHs is in the ball park of that predicted for the quiescent galaxies when the onset of quenching is at $z \sim 6.5$, and is higher for higher z_{quench} . (See also Fig. 3.)

by streams of higher angular momentum that naturally result in more extended galaxies. Furthermore, the high-sigma FFB galaxies, which are expected to suffer more frequent and stronger compaction events, are likely to go through blue-nugget phases where they are of high SFR and compact. On the other hand, the post-compaction galaxies tend to develop extended disks/rings from freshly accreted streams, in which the inward radial transport is suppressed by the massive bulge (Martig et al. 2009; Dekel et al. 2020b). Such galaxies may show a quiescent core and an extended envelope forming stars at a mild rate. The origin of this morphological variability or bimodality and its possible association with the bimodality between FFB and non-FFB galaxies is yet to be properly investigated.

7.2 Massive quiescent galaxies at cosmic morning

7.2.1 Galaxy properties and number densities

The dark matter fraction within the stellar effective radius can be an indicator of compaction events, which can be characteristic of galaxies on the FFB track. Pre-compaction, one expects that the dark matter dominates the central regions, but the compaction is expected to drive baryons into the center and generate baryon-dominated centers that soon become dominated by stars (Lapiner et al. 2023). This has been seen both in JWST observations and in the TNG50 simulations, with the transition typically at cosmic morning, $z \sim 6$ (de Graaff et al. 2024b).

The sizes of the post-FFB massive quiescent galaxies at cosmic morning are expected to be compact in most cases. Forming in high-sigma-peak halos by compaction of instreaming gas of low angular momentum, the star-forming FFB galaxies are expected to be compact, of sizes $\lesssim 300 \text{ pc}$ (Li et al. 2024, Fig. 10). The stellar systems formed may be expected to

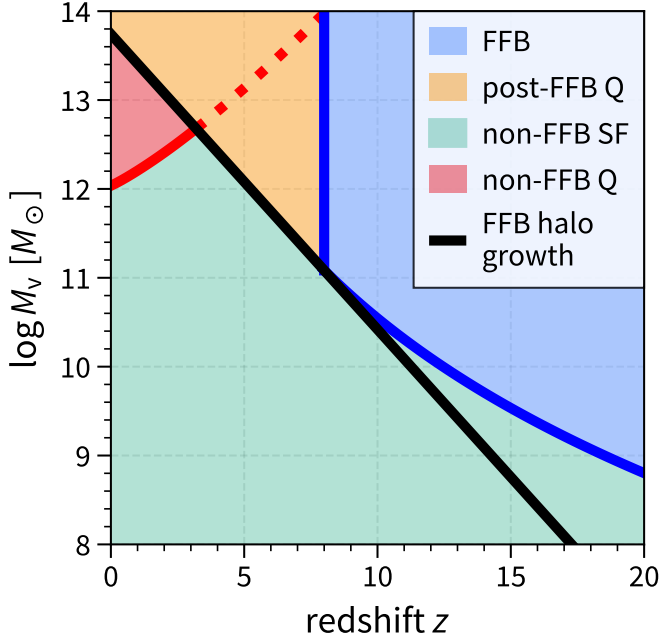


Figure 12. The division of galaxies into different zones in the plane of halo mass and redshift, to serve as the basis for the UVLFs shown in Fig. 13. The blue curves mark the threshold for FFB. Quenching is assumed in post-FFB galaxies at $z < z_{\text{quench}} = 8$. The black line represents the average mass growth of the fiducial FFB halo, the lowest-mass halo that evolves through an FFB phase (Fig. 2). At $z \gg 8$, all the galaxies are star forming, either FFB galaxies above the FFB threshold (blue shade) or non-FFB galaxies below the FFB threshold (green shade). At $z \leq 8$, the post-FFB galaxies, above the critical mass growth curve for FFB (orange shade), are quenched, while the non-FFB galaxies are star forming (green shade). Quenching is assumed by the UM model in high halo masses (above the red curve) independent of FFB, but the addition to the post-FFB quenching (red shade) is irrelevant in the redshift range of interest at cosmic morning.

remain compact in the subsequent quiescent phase when not many new stars are born. We note however that those galaxies that eventually develop extended disks may show somewhat larger effective radii. The current observations using JWST indicate that the quiescent galaxies at cosmic morning, $z > 3$, indeed tend to be very compact (Ji et al. 2024; Weibel et al. 2024; de Graaff et al. 2024a; Carnall et al. 2024).

Figure 10 shows the predicted stellar mass and UV magnitude of galaxies on the fiducial FFB evolutionary track as a function of redshift of observation. The onset of quenching is assumed to be at $z_{\text{quench}} = 6.5, 8$ or 10 . The growth in time at high z prior to the onset of quenching reflects the star formation in the FFB phase. The stellar mass is assumed to remain constant after z_{quench} , and the associated decline of brightness in time is due to passive evolution at the post-FFB quiescent phase.

Figure 11 shows the predicted number density of galaxies on the FFB (and post-FFB) evolutionary track, those that are brighter than the fiducial FFB galaxies, as a function of redshift. The onset of quenching is assumed to be either at $z_{\text{quench}} = 8$ or at $z_{\text{quench}} = 6.5$. We learn that the predicted number density of post-FFB quiescent galaxies at $z \sim 6$ is $n \gtrsim 10^{-5} \text{ Mpc}^{-3}$.

Also shown for comparison in Fig. 11 are number densities of AGN as observed by JWST (Harikane et al. 2023b) at

$z = 5-7$. They are observed in quiescent galaxies brighter than the corresponding predicted UV magnitude shown in Fig. 10 for galaxies on the fiducial FFB/non-FFB evolutionary track. We learn that the abundance of BHs is in the ballpark of that predicted for the quiescent galaxies when the onset of quenching is at $z \sim 6.5$, and is higher for higher z_{quench} .

7.2.2 UVLF for quiescent and star-forming galaxies

In order to compute the stellar mass function (SMF) and the UV luminosity function (UVLF) of the different galaxy types, Fig. 12 illustrates the division of the plane of halo mass versus redshift into three main zones: the star-forming FFB (ffb), the star-forming non-FFB (non), and the quiescent post-FFB (post).² Quenching is assumed in post-FFB galaxies at $z < z_{\text{quench}} = 8$. At $z > z_{\text{quench}}$, both the FFB and non-FFB galaxies are assumed to be star forming in their own manners, above and below the FFB threshold, respectively. At $z < z_{\text{quench}}$, the post-FFB galaxies, above the fiducial mass growth curve for FFB, are assumed to be quenched, while the non-FFB galaxies are still star forming. We allow smooth transition regions between the zones, as explained below.

In order to compute the stellar mass and UV magnitude of a galaxy at a point (M_v, z) , we derive the SFH along the halo growth trajectory leading to this point. For this we need the SFR at all points (M_v, z) along this trajectory, according to the zone they are in. The SFR in the main body of the FFB zone, SFR_{ffb} , is characterized by a global instantaneous star-formation efficiency (SFE) with respect to the baryonic accretion rate, ϵ_{ffb} , namely

$$\text{SFR}_{\text{ffb}} = \epsilon_{\text{ffb}} f_b \dot{M}_v. \quad (16)$$

On average, as long as the mean accretion rate and SFR do not vary too strongly, this instantaneous SFE is comparable to the global integrated SFE, namely $\epsilon_{\text{int}} = M_* / (f_b M_v)$, which is commonly deduced from observations. The fiducial value is $\epsilon_{\text{ffb}} = 0.3$, based on best fit to JWST observations at $z \sim 10$ (Li et al. 2024), but in principle it can range from 0.2 to unity and vary with redshift. The SFR in the main body of the post-FFB zone, SFR_{post} , is assumed to vanish. The SFR in the main body of the non-FFB zone, SFR_{non} , is adopted from the UniverseMachine (UM) model (Behroozi et al. 2019) as outlined in Li et al. (2024).

In order to allow smooth transitions between the zones, we consider a mixture of the components there, where the fraction of each, f_{type} is varied from unity in the main body of the associated zone to zero in the main body of the neighboring zone. In the transition from FFB to non-FFB we use f_{ffb} from Li et al. (2024). In the transition from FFB to post-FFB we similarly take f_{post} to be a sigmoid function centered at z_{quench} with a transition width $\Delta z = 0.2$ (full width $4 \Delta z$). The SFR of the mixture at (M_v, z) is then defined by

$$\text{SFR} = f_{\text{ffb}} [(1 - f_{\text{post}}) \text{SFR}_{\text{ffb}} + f_{\text{post}} \text{SFR}_{\text{post}}] + (1 - f_{\text{ffb}}) \text{SFR}_{\text{non}}. \quad (17)$$

For any given point (M_v, z) that contributes to the SMF and UVLF at z , the SFH is derived along the average halo

² A small fourth zone of non-FFB quenched galaxies in the top-left corner of Fig. 12 is not relevant in the redshift range considered here.

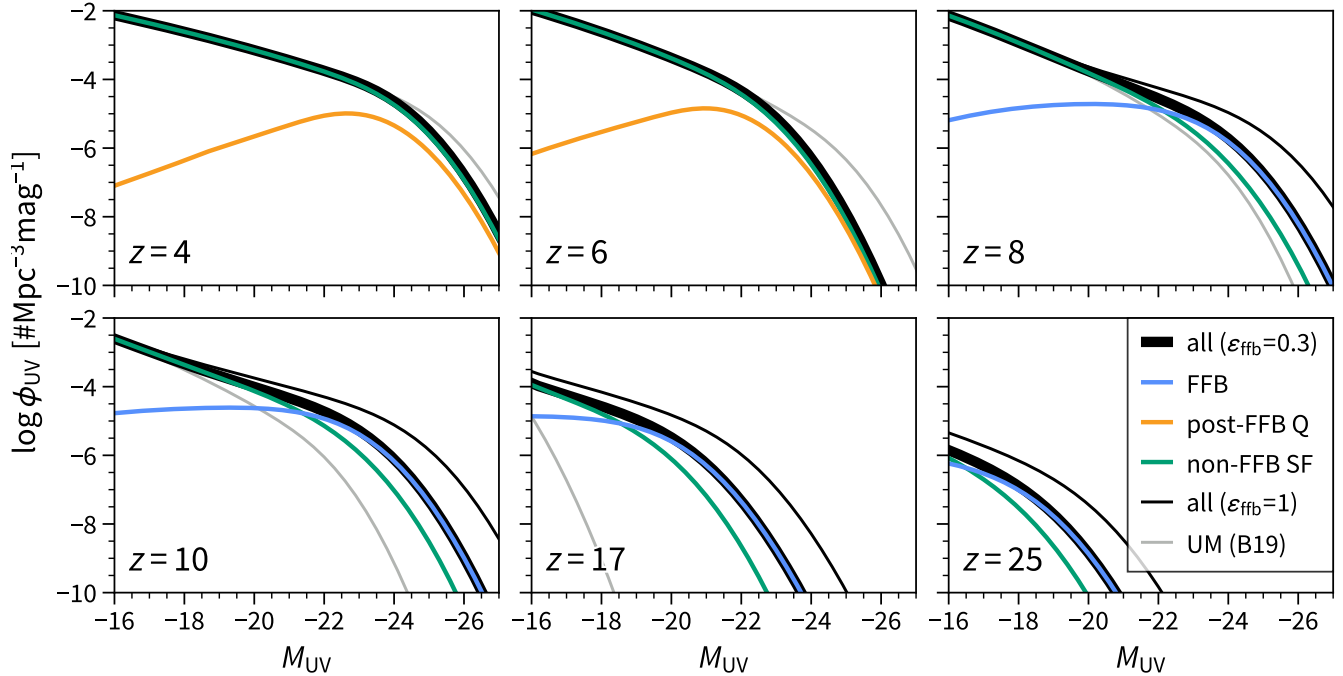


Figure 13. The predicted luminosity functions at different redshifts, at cosmic morning ($z=4, 6$) and cosmic dawn $z=8, 10, 17, 25$). The total LF with $\epsilon_{\text{ffb}}=0.3$ (black) is the sum of the LF for non-FFB galaxies (green) and the LF for FFB or post-FFB galaxies (blue and orange respectively). Here $z_{\text{quench}}=8$. Shown for comparison are the UM predictions (grey), which underestimate the LF at cosmic dawn. At $z \geq z_{\text{quench}}$, all the galaxies are star forming and the bright end is dominated by the FFB galaxies, above a threshold that declines from $M_{\text{UV}} \simeq -22$ at $z=8$ to $M_{\text{UV}} \simeq -18.5$ at $z=17$. The signature of the bimodality at cosmic dawn is not explicit; it is the bright-end excess of the LF due to the FFB galaxies. The total LF for $\epsilon_{\text{ffb}}=1$ is also shown at cosmic dawn (thin black); it may allow a better fit to the observational estimates at $z=17$ and 25 . Central to this figure is the prediction that at $z < z_{\text{quench}}$, the galaxies are divided to non-FFB star-forming galaxies (green) and post-FFB quenched galaxies (orange), with the star forming galaxies dominating the LF at all magnitudes. The LFs of the post-FFB quiescent galaxies at cosmic morning peak near $M_{\text{UV}} \simeq -22.7$ and $M_{\text{UV}} \simeq -21$ for $z=4$ and 6 respectively, where they contribute $\sim 10\%$ of the total LF (with $\epsilon_{\text{ffb}}=0.3$).

growth evolution track leading to this point, using eq. (1), making use of the SFR in the different zones along the track. The median stellar mass M_* is obtained by integrating the SFH over time. The median rest-frame UV magnitude M_{UV} at 1500 \AA is calculated from the SFH using the Flexible Stellar Population Synthesis (FSPS) code (Conroy et al. 2009), which naturally incorporates the fact that the stars in younger galaxies were brighter. We assume a Chabrier IMF (Chabrier 2003) and a metallicity of $0.1Z_{\odot}$. It is worth noting that the magnitudes used here are an improvement over the magnitudes derived in Li et al. (2024) from the stellar masses using a constant $M_{\text{UV}} - M_*$ relation. The SFH-based magnitudes are similar to the M_* -based magnitudes at $z < 10$, but they are higher at $z \geq 10$, by about one magnitude at $z \sim 15$ and two magnitudes at $z \sim 25$. This helps bringing the FFB-predicted LFs to better agreement with observed LFs at $z \sim 17$ and $z \sim 25$ (Pérez-González et al. 2025), though this is not the issue in the current paper which focuses on the post-FFB quiescent galaxies at cosmic morning.

Following Li et al. (2024), we introduce Gaussian-distribution scatter in the $M_* - M_V$ and $M_{\text{UV}} - M_V$ relations about the medians derived from the SFH, and obtain the conditional probabilities $p(\log M_* | M_V)$ and $p(M_{\text{UV}} | M_V)$.

The SMF and UVLF (marked F) at z are derived by a convolution of $p(F | M_V)$ with the halo mass function $n(M_V)$,

$$\phi(F) = \int p(F | M_V) n(M_V) dM_V. \quad (18)$$

This can be computed either for all the galaxies at z , or

separately for the two galaxy types (FFB and non-FFB at $z > z_{\text{quench}}$ or post-FFB and non-FFB at $z < z_{\text{quench}}$). In the transition zones, the integrand includes in addition the corresponding fraction of the number of the galaxy type of interest, which can be smaller than unity.

Figure 13 shows the predicted UV luminosity function (LF) at different redshifts during cosmic dawn and cosmic morning. The total LF is the sum of the LFs for galaxies on the two evolutionary tracks, namely, the non-FFB galaxies and the FFB/post-FFB galaxies. The onset of post-FFB quenching is assumed here to be at $z_{\text{quench}}=8$ and the SFE is at the fiducial value $\epsilon_{\text{ffb}}=0.3$.

At $z \geq z_{\text{quench}}=8$, all the galaxies of the two types are star forming and the bright end of the LF is dominated by the bursting FFB galaxies, above a threshold that declines from $M_{\text{UV}} \simeq -22$ at $z=8$ to $M_{\text{UV}} \simeq -18.5$ at $z=17$. One can see that the signature of the bimodality at cosmic dawn is not pronounced; it is reflected in the bright-end excess of the LF due to the FFB galaxies. Shown for comparison are the extrapolated UM predictions, which underestimate the LF at cosmic dawn. The non-FFB LF is higher than the UM predictions due to inclusion of FFB galaxies in the smooth transition region between the FFB and non-FFB zones. The total LF for a higher SFE, $\epsilon_{\text{ffb}}=1$, is also shown at cosmic dawn. Being higher than the LF for $\epsilon_{\text{ffb}}=0.3$, it may allow a better fit to the observational estimates at $z=17$ and 25 (Pérez-González et al. 2025).

At $z < z_{\text{quench}}$, the galaxies are divided to non-FFB star-

forming galaxies and post-FFB quenched galaxies. In this redshift range, the star-forming galaxies dominate the LF at all magnitudes. The LFs of quiescent galaxies peak at $M_{\text{UV}} \simeq -22.7$ and $M_{\text{UV}} \simeq -21$ for $z=4$ and 6 , respectively, and they are $\sim 10\%$ of the total LF at the peak in this redshift range. The predicted LF of the quiescent galaxies from Fig. 13 is to be compared to the LF of the quiescent, red, compact galaxies as observed at cosmic morning (§ 1.2, Fig. 1).

Compared to the pre-JWST UM predictions, our model with $\epsilon_{\text{ff}}=0.3$ produces a higher number density of bright galaxies at $z > z_{\text{quench}}$ due to the enhanced SFE in the FFB zone and the transition region into the non-FFB zone. At lower redshifts, $z < z_{\text{quench}}$, the introduction of post-FFB quenching suppresses the bright end of the UVLF relative to the continuous star formation in the standard UM model.

The SMFs, which are not shown here, are qualitatively similar to the UVLFs. The main difference is that at $z \lesssim z_{\text{quench}}$ the post-FFB quiescent galaxies become the dominant component in the SMF, e.g., for $M_* > 10^{10.3} M_{\odot}$ at $z=6$, because they retain the high stellar masses while their luminosities begin to fade by quenching.

8 CONCLUSION

We argue (largely based on Fig. 2) that the early evolution of galaxies at high redshifts is bimodal as a function of halo mass, or equivalently the associated height of the peaks in the density fluctuation field. The evolutionary track of massive halos goes through an FFB phase. It connects the observed excess of bright galaxies at cosmic dawn ($z > 8$) to the observed excess of massive quiescent galaxies and the presence of supermassive black holes with high BH-to-stellar mass ratio at cosmic morning ($z \sim 4-7$). On the other evolutionary track, consisting of lower-mass, more abundant halos, the galaxies avoid the FFB phase. Their stellar growth is expected to be gradual, eventually leading to the peak of star-forming galaxies at cosmic noon ($z \sim 1-3$).

As seen in Fig. 2, the massive track consists of dark-matter halos that are more massive than $\sim 10^{10.5} M_{\odot}$ at $z = 10$ and represent $\geq 4\sigma$ peaks in the density fluctuation field. These halos undergo a phase of feedback-free starbursts (FFB) with high star-formation efficiency in thousands of dense star clusters within each compact galaxy (Dekel et al. 2023; Li et al. 2024). The less massive, $2-3\sigma$ peak halos avoid the FFB phase and form stars gradually through cosmic dawn and cosmic morning subject to stellar feedback.

The key question addressed is the origin of efficient quenching of star formation preferably in post FFB galaxies. We propose that the post-FFB galaxies quench soon after the FFB phase and remain quiescent due to the combined effect of several mechanisms:

- Gas depletion from the ISM by the FFB starbursts and the associated outflows (Li et al. 2024) suppresses the available local gas supply immediately available for further star formation.
- The high-sigma-peak FFB halos suffer excessive compaction events driven by angular-momentum loss in colliding streams and enhanced frequency of mergers (Dubois et al. 2012). The compaction events drive quenching by several different ways, including (a) further gas consumption,

(b) formation of extended, non-contracting disk and ring, (c) compaction-driven black-hole growth that boosts AGN feedback, and (d) driving stream-disrupting turbulence in the CGM.

- The disruption of the inflowing cold streams is a key for the required complete quenching at cosmic morning, and it poses a non-trivial open challenge. We assess that possible mechanisms for stream disruption are supersonic turbulence in the CGM (possibly generated by AGN feedback) and photo-heating of the stream-CGM mixing layer by AGN radiation.
- Simulations show that AGN feedback is necessary for complete quenching. This could be, e.g., by generating CGM turbulence or indirect photo-heating. The FFB phase is indeed expected to lead to rapid growth of BH seeds and subsequent growth to supermassive BHs that allow enhanced AGN feedback (Dekel et al. 2025).

The bimodality to FFB and non-FFB evolutionary tracks, and the post-FFB quenching, are yet to be investigated in proper cosmological simulations that resolve the FFB processes at cosmic dawn with ~ 1 pc resolution and continue to cosmic morning while incorporating black hole growth and AGN feedback.

Based on the above discussion of post-FFB evolution, one can deduce observable predictions for the quiescent galaxies at cosmic morning. They are expected to be massive, compact, dominated by stars, and possibly showing signatures of outflows and AGN. Their comoving number density is expected to be $\gtrsim 10^{-5} \text{ Mpc}^{-3}$, comparable to the density of super-bright FFB galaxies at cosmic dawn, and to the density of black holes at cosmic morning. The UV luminosity function of post-FFB quiescent galaxies at cosmic morning is expected to peak near $M_{\text{UV}} \sim -22.7$ and -21 at $z \sim 4$ and 6 , respectively, and to contribute about 10% to the total LF at these peak magnitudes, respectively.

ACKNOWLEDGMENTS

We are grateful for stimulating discussions with Anna de Graaff, David Elbaz, Yuchi Harikane, Joel Primack, Volker Springel, Sandro Tacchella and Andrea Weibel. Yuchi Harikane provided the number densities for BHs shown in Fig. 3 and Fig. 11, given the post-FFB UV magnitudes predicted. This work was supported by the Israel Science Foundation Grant ISF 861/20, and by the US National Science Foundation - US-Israel Bi-national Science Foundation grants 2023730 (with Romain Teyssier) and 2023723 (with Frank van den Bosch). NM acknowledges support from the Israel Science Foundation grant ISF 3061/21. ZL acknowledges funding from the European Union’s Horizon 2020 research and innovation programme under the Marie Skłodowska-Curie grant agreement No 101109759 (“CuspCore”).

DATA AVAILABILITY

Data and results underlying this article will be shared on reasonable request to the corresponding author.

REFERENCES

- Adamo A., et al., 2024, *Nature*, **632**, 513
- Adams N. J., et al., 2023, *MNRAS*, **518**, 4755
- Andalman Z. L., Teyssier R., Dekel A., 2024, *arXiv e-prints*, p. [arXiv:2410.20530](https://arxiv.org/abs/2410.20530)
- Antwi-Danso J., et al., 2025, *ApJ*, **978**, 90
- Arrabal Haro P., Dickinson M., Finkelstein S. L., Fujimoto S., Fernández V., Kartaltepe J. S., Jung I., et al. 2023, *ApJ*, **951**, L22
- Aung H., Mandelker N., Nagai D., Dekel A., Birnboim Y., 2019, *MNRAS*, **490**, 181
- Aung H., Mandelker N., Dekel A., Nagai D., Semenov V., van den Bosch F. C., 2024, *MNRAS*, **532**, 2965
- Banik U., van den Bosch F. C., 2021, *ApJ*, **912**, 43
- Bardeen J. M., Bond J. R., Kaiser N., Szalay A. S., 1986, *ApJ*, **304**, 15
- Barro G., et al., 2013, *ApJ*, **765**, 104
- Barro G., et al., 2017, *ApJ*, **840**, 47
- Begelman M. C., Blandford R. D., Rees M. J., 1980, *Nature*, **287**, 307
- Behroozi P. S., Wechsler R. H., Conroy C., 2013, *ApJ*, **762**, L31
- Behroozi P., Wechsler R. H., Hearin A. P., Conroy C., 2019, *MNRAS*, **488**, 3143
- Belli S., et al., 2024, *Nature*, **630**, 54
- Benitez-Llambay A., Frenk C., 2020, *MNRAS*, **498**, 4887
- Bennett J. S., Sijacki D., 2020, *MNRAS*, **499**, 597
- Berlok T., Pfrommer C., 2019, *MNRAS*, **489**, 3368
- Birnboim Y., Dekel A., 2003, *MNRAS*, **345**, 349
- Blank M., Macciò A. V., Dutton Aaron A. and Obreja A., 2019, *MNRAS*, **487**, 5476
- Blecha L., Loeb A., 2008, *MNRAS*, **390**, 1311
- Bond J. R., Cole S., Efstathiou G., Kaiser N., 1991, *ApJ*, **379**, 440
- Bouwens R., Illingworth G., Oesch P., Stefanon M., Naidu R., van Leeuwen L., Magee D., 2023, *MNRAS*, **523**, 1009
- Boylan-Kolchin M., 2023, *Nature Astronomy*, **7**, 731
- Carnall A. C., et al., 2023a, *MNRAS*, **520**, 3974
- Carnall A. C., et al., 2023b, *Nature*, **619**, 716
- Carnall A. C., et al., 2024, *MNRAS*, **534**, 325
- Ceverino D., Klypin A., 2009, *ApJ*, **695**, 292
- Ceverino D., Klypin A., Klimek E. S., Trujillo-Gomez S., Churchill C. W., Primack J., Dekel A., 2014, *MNRAS*, **442**, 1545
- Chabrier G., 2003, *PASP*, **115**, 763
- Claeysens A., Adamo A., Richard J., Mahler G., Messa M., Dessauges-Zavatsky M., 2023, *MNRAS*, **520**, 2180
- Codis S., Pichon C., Devriendt J., Slyz A., Pogosyan D., Dubois Y., Sousbie T., 2012, *MNRAS*, **427**, 3320
- Codis S., Pogosyan D., Pichon C., 2018, *MNRAS*, **479**, 973
- Conroy C., Gunn J. E., White M., 2009, *ApJ*, **699**, 486
- D'Eugenio F., et al., 2024, *Nature Astronomy*, **8**, 1443
- Daddi E., et al., 2022a, *A&A*, **661**, L7
- Daddi E., et al., 2022b, *ApJ*, **926**, L21
- Dekel A., Birnboim Y., 2006, *MNRAS*, **368**, 2
- Dekel A., Silk J., 1986, *ApJ*, **303**, 39
- Dekel A., et al., 2009, *Nature*, **457**, 451
- Dekel A., Zolotov A., Tweed D., Cacciato M., Ceverino D., Primack J. R., 2013, *MNRAS*, **435**, 999
- Dekel A., Lapiner S., Dubois Y., 2019, *arXiv e-prints*, p. [arXiv:1904.08431](https://arxiv.org/abs/1904.08431)
- Dekel A., Ginzburg O., Jiang F., Freundlich J., Lapiner S., Ceverino D., Primack J., 2020a, *MNRAS*, **493**, 4126
- Dekel A., et al., 2020b, *MNRAS*, **496**, 5372
- Dekel A., Sarkar K. C., Birnboim Y., Mandelker N., Li Z., 2023, *MNRAS*, **523**, 3201
- Dekel A., Stone N. C., Dutta Chowdhury D., Gilbaum S., Li Z., Mandelker N., van den Bosch F. C., 2025, *A&A*, **695**, A97
- Donnan C. T., et al., 2023a, *MNRAS*, **518**, 6011
- Donnan C. T., McLeod D. J., McLure R. J., Dunlop J. S., Carnall A. C., Cullen F., Magee D., 2023b, *MNRAS*, **520**, 4554
- Dubois Y., Pichon C., Haehnelt M., Kimm T., Slyz A., Devriendt J., Pogosyan D., 2012, *MNRAS*, **423**, 3616
- Dubois Y., Peirani S., Pichon h., Devriendt J., Gavazzi R., Welker Chard Volonteri M., 2016, *MNRAS*, **463**, 3948
- Dubois Y., et al., 2021, *A&A*, **651**, A109
- Dutta Chowdhury D., Dekel A., Mandelker N., Ginzburg O., Genzel R., 2024, *arXiv e-prints*, p. [arXiv:2409.01589](https://arxiv.org/abs/2409.01589)
- Fall S. M., Efstathiou G., 1980, *MNRAS*, **193**, 189
- Farina E. P., et al., 2022, *ApJ*, **941**, 106
- Ferland G. J., et al., 2017, *Rev. Mex. Astron. Astrofis.*, **53**, 385
- Ferrara A., Pallottini A., Dayal P., 2023, *MNRAS*, **522**, 3986
- Fielding D. B., Ostriker E. C., Bryan G. L., Jermyn A. S., 2020, *ApJ*, **894**, L24
- Finkelstein S. L., Bagley M. B., Arrabal Haro P., CEERS 2022, *ApJ*, **940**, L55
- Finkelstein S. L., Bagley M. B., Ferguson H. C., CEERS 2023, *ApJ*, **946**, L13
- Fiore F., Ferrara A., Bischetti M., Feruglio C., Travascio A., 2023, *ApJ*, **943**, L27
- Förster Schreiber N. M., Renzini A., Mancini C., Genzel R., Bouché N., Cresci G., Hicks E. K. S., et al. 2018, *ApJS*, **238**, 21
- Förster Schreiber N. M., et al., 2019, *ApJ*, **875**, 21
- Fujimoto S., et al., 2024, *arXiv e-prints*, p. [arXiv:2402.18543](https://arxiv.org/abs/2402.18543)
- Gabor J. M., Bournaud F., 2014, *MNRAS*, **437**, L56
- Ginzburg O., Dekel A., Mandelker N., Krumholz M. R., 2022, *MNRAS*, **513**, 6177
- Ginzburg O., Dekel A., Mandelker N., Dutta Chowdhury D., Bournaud F., Ceverino D., Primack J., 2025, *arXiv e-prints*, p. [arXiv:2501.07097](https://arxiv.org/abs/2501.07097)
- Goerdt T., Moore B., Read J. I., Stadel J., Zemp M., 2006, *MNRAS*, **368**, 1073
- Gronke M., Oh S. P., 2018, *MNRAS*, **480**, L111
- Gronke M., Oh S. P., 2020a, *MNRAS*, **492**, 1970
- Gronke M., Oh S. P., 2020b, *MNRAS*, **494**, L27
- Gronke M., Oh S. P., Ji S., Norman C., 2022, *MNRAS*, **511**, 859
- Grudić M. Y., Hopkins P. F., 2023, *arXiv e-prints*, p. [arXiv:2308.16268](https://arxiv.org/abs/2308.16268)
- Hachisu I., 1979, *PASJ*, **31**, 523
- Harikane Y., et al., 2023a, *ApJS*, **265**, 5
- Harikane Y., et al., 2023b, *ApJ*, **959**, 39
- Harikane Y., et al., 2025, *ApJ*, **980**, 138
- Haslbauer M., Kroupa P., Zonoozi A. H., Haghi H., 2022, *ApJ*, **939**, L31
- Heckman T. M., Best P. N., 2014, *ARA&A*, **52**, 589
- Huertas-Company M., et al., 2018, *ApJ*, **858**, 114
- Inayoshi K., Harikane Y., Inoue A. K., Li W., Ho L. C., 2022, *ApJ*, **938**, L10
- Inoue S., Dekel A., Mandelker N., Ceverino D., Bournaud F., Primack J., 2016, *MNRAS*, **456**, 2052
- Ji S., Oh S. P., Masterson P., 2019, *MNRAS*, **487**, 737
- Ji Z., et al., 2024, *arXiv e-prints*, p. [arXiv:2401.00934](https://arxiv.org/abs/2401.00934)
- Jiang F., et al., 2019, *MNRAS*, **488**, 4801
- Kanjilal V., Dutta A., Sharma P., 2021, *MNRAS*, **501**, 1143
- Katz H., et al., 2020, *MNRAS*, **494**, 2200
- Kaul I., Tan B., Oh S. P., Mandelker N., 2025, *MNRAS*, **523**, 3201
- Kaur K., Sridhar S., 2018, *ApJ*, **868**, 134
- Kereš D., Katz N., Weinberg D. H., Davé R., 2005, *MNRAS*, **363**, 2
- Kereš D., Katz N., Fardal M., Davé R., Weinberg D. H., 2009, *MNRAS*, **395**, 160
- Klypin A., et al., 2021, *MNRAS*, **504**, 769
- Kravtsov A. V., Klypin A. A., Khokhlov A. M., 1997, *ApJS*, **111**, 73
- Labbé I., et al., 2023, *Nature*, **616**, 266
- Lapiner S., Dekel A., Dubois Y., 2021, *MNRAS*, **505**, 172
- Lapiner S., et al., 2023, *MNRAS*, **522**, 4515
- Li Z., Dekel A., Sarkar K. C., Aung H., Gialvalisco M., Mandelker N., Tacchella S., 2024, *A&A*, **690**, A108
- Lochhaas C., Tumlinson J., O'Shea B. W., Peeples M. S., Smith B. D., Werk J. K., Augustin R., Simons R. C., 2021, *ApJ*, **922**, 121
- Lovell C. C., Harrison I., Harikane Y., Tacchella S., Wilkins S. M., 2023, *MNRAS*, **518**, 2511
- Lu Y. S., Mandelker N., Oh S. P., Dekel A., van den Bosch F. C., Springel V., Nagai D., van de Voort F., 2024, *MNRAS*, **527**, 11256
- Madau P., Dickinson M., 2014, *ARA&A*, **52**, 415
- Madau P., Quataert E., 2004, *ApJ*, **606**, L17
- Maiolino R., et al., 2024, *A&A*, **691**, A145

- Mandelker N., Padnos D., Dekel A., Birnboim Y., Burkert A., Krumholz M. R., Steinberg E., 2016, *MNRAS*, **463**, 3921
- Mandelker N., van Dokkum P. G., Brodie J. P., van den Bosch F. C., Ceverino D., 2018, *ApJ*, **861**, 148
- Mandelker N., Nagai D., Aung H., Dekel A., Padnos D., Birnboim Y., 2019, *MNRAS*, **484**, 1100
- Mandelker N., Nagai D., Aung H., Dekel A., Birnboim Y., van den Bosch F. C., 2020a, *MNRAS*, **494**, 2641
- Mandelker N., van den Bosch F. C., Nagai D., Dekel A., Birnboim Y., Aung H., 2020b, *MNRAS*, **498**, 2415
- Mandelker N., van den Bosch F. C., Springel V., van de Voort F., Burchett J. N., Butsky I. S., Nagai D., Oh S. P., 2021, *ApJ*, **923**, 115
- Mandelker N., Ginzburg O., Dekel A., Bournaud F., Krumholz M. R., Ceverino D., Primack J., 2025, *MNRAS*, **538**, L9
- Martig M., Bournaud F., Teyssier R., Dekel A., 2009, *ApJ*, **707**, 250
- Mason C. A., Trenti M., Treu T., 2023, *MNRAS*, **521**, 497
- Mayer L., van Dokkum P. G., Messa M., Capelo P. R., Adamo A., 2024, *arXiv e-prints*, p. [arXiv:2411.00670](https://arxiv.org/abs/2411.00670)
- McCourt M., Oh S. P., O'Leary R., Madigan A.-M., 2018, *MNRAS*, **473**, 5407
- Menon S. H., Federrath C., Krumholz M. R., 2023, *MNRAS*, **521**, 5160
- Menon S. H., Lancaster L., Burkhart B., Somerville R. S., Dekel A., Krumholz M. R., 2024, *ApJ*, **967**, L28
- Messa M., Dessauges-Zavadsky M., Adamo A., Richard J., Claeysens A., 2024, *MNRAS*, **529**, 2162
- Moster B. P., Naab T., White S. D. M., 2018, *MNRAS*, **477**, 1822
- Mowla L., et al., 2024, *arXiv e-prints*, p. [arXiv:2402.08696](https://arxiv.org/abs/2402.08696)
- Naidu R. P., et al., 2022, *ApJ*, **940**, L14
- Ono Y., Ouchi M., Harikane Y., Yajima H., Nakajima K., Fujimoto S., Nakane M., Xu Y., 2025, *arXiv e-prints*, p. [arXiv:2502.08885](https://arxiv.org/abs/2502.08885)
- Onoue M., et al., 2024, *arXiv e-prints*, p. [arXiv:2409.07113](https://arxiv.org/abs/2409.07113)
- Ostriker J., 1964, *ApJ*, **140**, 1056
- Padnos D., Mandelker N., Birnboim Y., Dekel A., Krumholz M. R., Steinberg E., 2018, *MNRAS*, **477**, 3293
- Pérez-González P. G., Costantin L., Langerodi D., Rinaldi P., Annunziatella M., Ilbert O., Colina L., et al. 2023, *ApJ*, **951**, L1
- Pérez-González P. G., et al., 2025, *arXiv e-prints*, p. [arXiv:2503.15594](https://arxiv.org/abs/2503.15594)
- Press W. H., Schechter P., 1974, *ApJ*, **187**, 425
- Read J. I., Goerdt T., Moore B., Pontzen A. P., Stadel J., Lake G., 2006, *MNRAS*, **373**, 1451
- Reines A. E., Volonteri M., 2015, *ApJ*, **813**, 82
- Setton D. J., et al., 2024, *ApJ*, **974**, 145
- Sparre M., Pfrommer C., Ehlert K., 2020, *MNRAS*, **499**, 4261
- Steinhardt C. L., Kokorev V., Rusakov V., Garcia E., Sneppen A., 2023, *ApJ*, **951**, L40
- Sun G., Faucher-Giguère C.-A., Hayward C. C., Shen X., 2023a, *MNRAS*, **526**, 2665
- Sun G., Faucher-Giguère C.-A., Hayward C. C., Shen X., Wetzel A., Cochrane R. K., 2023b, *ApJ*, **955**, L35
- Tacchella S., Dekel A., Carollo C. M., Ceverino D., DeGraf C., Lapiner S., Mandelker N., Primack Joel R., 2016a, *MNRAS*, **457**, 2790
- Tacchella S., Dekel A., Carollo C. M., Ceverino D., DeGraf C., Lapiner S., Mandelker N., Primack J. R., 2016b, *MNRAS*, **458**, 242
- Tacchella S., et al., 2023, *arXiv e-prints*, p. [arXiv:2302.07234](https://arxiv.org/abs/2302.07234)
- Tan B., Oh S. P., Gronke M., 2021, *MNRAS*, **502**, 3179
- Teyssier R., 2002, *A&A*, **385**, 337
- Tomassetti M., et al., 2016, *MNRAS*, **458**, 4477
- Trakhtenbrot B., Netzer H., Lira P., Shemmer O., 2011, *ApJ*, **730**, 7
- Übler H., et al., 2023, *A&A*, **677**, A145
- Valentino F., et al., 2025, *arXiv e-prints*, p. [arXiv:2503.01990](https://arxiv.org/abs/2503.01990)
- Vanzella E., et al., 2023, *ApJ*, **945**, 53
- Wang B., et al., 2024, *ApJ*, **969**, L13
- Watson W. A., Iliev I. T., D'Aloisio A., Knebe A., Shapiro P. R., Yepes G., 2013, *MNRAS*, **433**, 1230
- Wechsler R. H., Bullock J. S., Primack J. R., Kravtsov A. V., Dekel A., 2002, *ApJ*, **568**, 52
- Weibel A., et al., 2024, *arXiv e-prints*, p. [arXiv:2409.03829](https://arxiv.org/abs/2409.03829)
- Wilkins S. M., et al., 2023, *MNRAS*, **519**, 3118
- Yang Y., Ji S., 2023, *MNRAS*, **520**, 2148
- Yao Z., Mandelker N., Oh S. P., Aung H., Dekel A., 2025, *MNRAS*, **536**, 3053
- Yung L. Y. A., Somerville R. S., Finkelstein S. L., Wilkins S. M., Gardner J. P., 2024, *MNRAS*, **527**, 5929
- Zackrisson E., Rydberg C.-E., Schaerer D., Östlin G., Tuli M., 2011, *ApJ*, **740**, 13
- Zhao D. H., Jing Y. P., Mo H. J., Börner G., 2009, *ApJ*, **707**, 354
- Ziparo F., Ferrara A., Sommovigo Laura and Kohandel M., 2023, *MNRAS*, **520**, 2445
- Zolotov A., et al., 2015, *MNRAS*, **450**, 2327
- de Graaff A., et al., 2024a, *Nature Astronomy*,
- de Graaff A., Pillepich A., Rix H.-W., 2024b, *ApJ*, **967**, L40
- van Dokkum P. G., et al., 2015, *ApJ*, **813**, 23